Article

Pliocene decoupling of equatorial Pacific temperature and pH gradients

https://doi.org/10.1038/s41586-021-03884-7

Received: 29 November 2020

Accepted: 6 August 2021

Published online: 20 October 2021

Check for updates

Madison G. Shankle[1,2]✉, Natalie J. Burls[3], Alexey V. Fedorov[1,4], Matthew D. Thomas[1,5], Wei Liu[6], Donald E. Penman[1,7], Heather L. Ford[8], Peter H. Jacobs[9,10], Noah J. Planavsky[1] & Pincelli M. Hull[1]✉

Ocean dynamics in the equatorial Pacific drive tropical climate patterns that affect marine and terrestrial ecosystems worldwide. How this region will respond to global warming has profound implications for global climate, economic stability and ecosystem health. As a result, numerous studies have investigated equatorial Pacific dynamics during the Pliocene (5.3–2.6 million years ago) and late Miocene (around 6 million years ago) as an analogue for the future behaviour of the region under global warming[1–12]. Palaeoceanographic records from this time present an apparent paradox with proxy evidence of a reduced east–west sea surface temperature gradient along the equatorial Pacific[1,3,7,8]—indicative of reduced wind-driven upwelling—conflicting with evidence of enhanced biological productivity in the east Pacific[13–15] that typically results from stronger upwelling. Here we reconcile these observations by providing new evidence for a radically different-from-modern circulation regime in the early Pliocene/late Miocene[16] that results in older, more acidic and more nutrient-rich water reaching the equatorial Pacific. These results provide a mechanism for enhanced productivity in the early Pliocene/late Miocene east Pacific even in the presence of weaker wind-driven upwelling. Our findings shed new light on equatorial Pacific dynamics and help to constrain the potential changes they will undergo in the near future, given that the Earth is expected to reach Pliocene-like levels of warming in the next century.

A salient feature of the modern tropical Pacific climate is a pronounced zonal (east–west) sea surface temperature (SST) gradient along the equator, with mean temperature decreasing from around 29 °C in the western Pacific warm pool to around 23 °C in the eastern Pacific equatorial cold tongue[2]. This zonal SST gradient is tightly coupled to the Pacific zonal atmospheric circulation—known as the Walker cell—whose winds in turn control the zonal tilt of the oceanic thermocline and the strength of equatorial upwelling via the Bjerknes feedback[17]. The Pacific zonal SST gradient thus plays a key role in defining the climate of the tropics. Variations in this gradient produce the El Niño–Southern Oscillation—a dominant mode of interannual climate variability in the tropics and beyond[18]. In addition, vigorous upwelling in the eastern tropical Pacific brings low-pH, nutrient-rich water up into the surface ocean, supporting highly productive marine ecosystems that are important to the economic health and food security of adjacent nations[19,20].

Despite the importance of the Pacific zonal SST gradient for climate and marine ecosystems, considerable uncertainty persists in how this ocean feature will respond to global warming[21]. One approach is to turn to past warm climates such as the Pliocene epoch (5.3–2.6 million years ago (Ma))—the last time in Earth's history when atmospheric CO_2 concentrations were similar (300–450 ppm) to the anthropogenically forced levels seen today[10,22]. By investigating Earth's climate during past warm periods such as the Pliocene (~2–4 °C warmer temperatures than modern[23–28]) and indeed even the latest Miocene (~6 Ma, ~5 °C warmer[29]), it is possible to develop a better understanding of tropical Pacific dynamics during warmer near-equilibrium climate states.

Existing records of the early Pliocene and late Miocene equatorial Pacific present a paradox. Today, a decrease in the zonal temperature gradient corresponds to reduced biological productivity in the eastern equatorial Pacific owing to reduced wind-driven upwelling of nutrient-rich waters—as occurs during an El Niño event. Perplexingly, records from the Pliocene and late Miocene seem to show a decoupling between the zonal SST gradient and biological productivity—with evidence for decreased zonal SST gradients[1,3,7,8] but increased productivity[13–15]. One solution to this paradox would be for the upwelled water to have been more nutrient-rich relative to modern, such that a smaller volume of upwelled water would support greater productivity.

Here we use the boronpH proxy to reconstruct the evolution of the Pacific zonal pH gradient along the equator since the late Miocene to test this idea that circulation changes delivered older, more nutrient-rich water to the eastern equatorial Pacific (EEP). This test relies on the fact that deep water that is upwelled to the surface contains

[1]Department of Earth and Planetary Sciences, Yale University, New Haven, CT, USA. [2]School of Earth and Environmental Sciences, University of St Andrews, St Andrews, UK. [3]Department of Atmospheric, Oceanic and Earth Sciences, George Mason University, Fairfax, VA, USA. [4]LOCEAN/IPSL, Sorbonne University, Paris, France. [5]University Corporation for Atmospheric Research, Boulder, CO, USA. [6]Department of Earth and Planetary Sciences, University of California, Riverside, CA, USA. [7]Department of Geosciences, Utah State University, Logan, UT, USA. [8]School of Geography, Queen Mary University of London, London, UK. [9]Department of Environmental Science and Policy, George Mason University, Fairfax, VA, USA. [10]NASA Goddard Space Flight Center, Greenbelt, MD, USA. ✉e-mail: mgs23@st-andrews.ac.uk; pincelli.hull@yale.edu

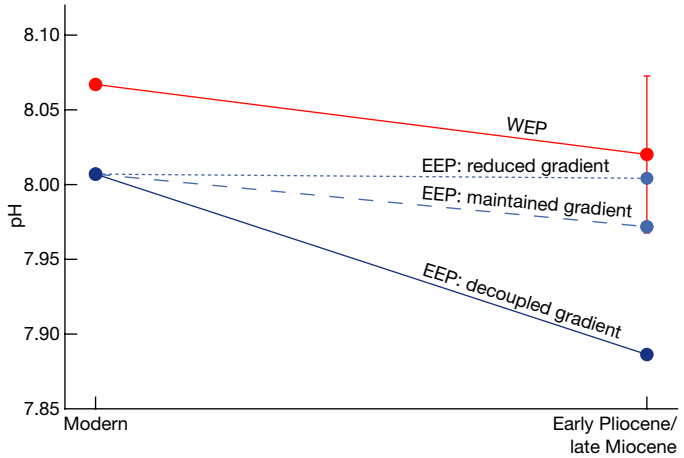

Fig. 1 | Different paradigms of Pliocene climate (degree of reduction in the zonal sea surface temperature gradient) predict different changes in zonal pH gradient. Red: modern western equatorial Pacific (WEP) pH (~8.067, average over the 25–50 m depth range) and average ~6 Ma pH from this study (proxy data, ~8.02, with 2σ). Blue lines represent different scenarios for eastern equatorial Pacific (EEP) pH change relative to modern (~8.007, average over the 25–50 m depth range). Blue dots: coupled reduction in zonal temperature and pH gradients (that is, the same fractional change) with thermal gradient reduction as in Liu and colleagues[31]. Blue dashes: coupled reduction but with lesser thermal gradient reduction as in Zhang and colleagues[3]. Blue solid: modelled ~6 Ma pH from this study (~7.886, average over the 25–50 m depth range) reflecting decoupled changes in temperature and pH gradients.

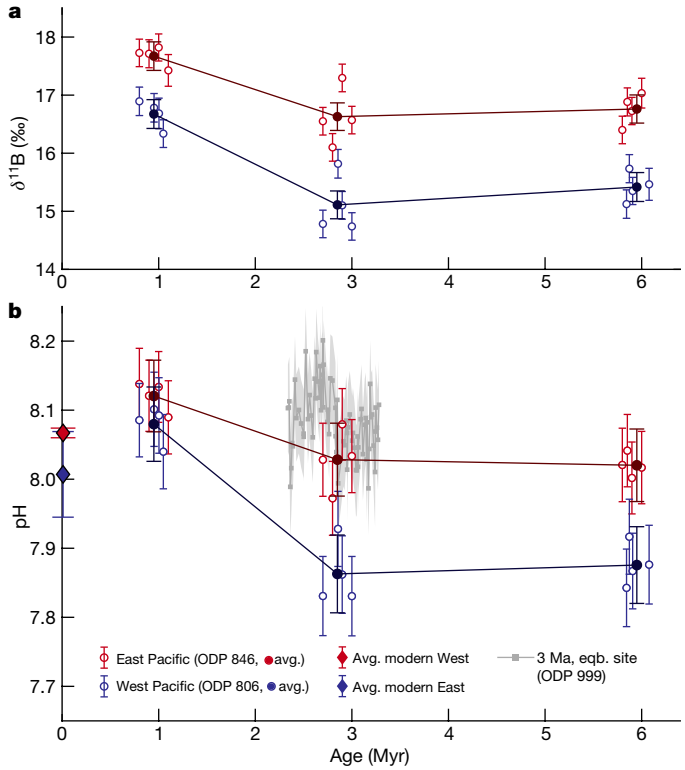

Fig. 2 | δ^{11}B-reconstructed pH shows an enhanced zonal pH gradient relative to modern at around 3 Ma and around 6 Ma. a, Boron isotopic composition of *O. universa* from the east (blue) and west (red) equatorial Pacific with 2σ analytical uncertainty (empty circles; averages at ~1 Ma, ~3 Ma and ~6 Ma in filled circles). **b**, δ^{11}B-derived pH with 2σ from a Monte Carlo (10,000 replicates) simulation (empty circles; averages in filled circles). Additional pH data included for context are: modern observational pH averaged over 25–50 m (the depth habitat of *O. universa*) with 1σ (diamonds) and δ^{11}B-derived pH with 95% confidence intervals from a site in equilibrium with the atmosphere[51] (eqb. site) (grey points and shading, central Caribbean ODP Site 999, from *Globigerinoides ruber*).

more nutrients than surface water owing to the remineralization of organic matter, which liberates nutrients along with CO_2, resulting in a decrease in the upwelled water's pH. As a result, the upwelling of older water masses contributes proportionately more acidity and nutrients to the surface, owing to their prolonged accumulation of respired organic matter. There are four primary, but not necessarily mutually exclusive, ways to upwell relatively older water into the EEP: (1) the water mass source could be further away, (2) the path to the EEP could be longer, (3) the flow could be slower, and/or (4) the water mass could upwell from deeper depths with relatively older water.

We focus our efforts on pH as there is an ongoing debate as to the magnitude of the zonal temperature gradient reduction at the time, with estimates for the reduction ranging from around 1 °C (refs. [3,6,11]) to around 3.5 °C (refs. [1,4,10,12,30,31]) relative to modern, depending on the proxy, calibration, sites used and time interval of focus. Although the magnitude is debated, all SST studies suggest that the Pliocene/late Miocene climate was characterized by a reduced zonal temperature gradient and a deeper/warmer thermocline relative to modern[1–4,6,9,10,31,32]—suggestive of a more El Niño-like background state or 'El Padre'[1,5,12,33]. Any reduction in the zonal SST gradient would seem to contradict records of high primary production in the east Pacific at this time[13–15].

While it is difficult to reconstruct nutrient delivery in upwelling areas, the boron isotopic (δ^{11}B) composition of planktonic foraminifera provides a robust pH proxy for tracing changes in the chemical composition of seawater though time[34,35]. Critically, different paradigms of Pliocene climate, in which physical (SST) and biogeochemical (pH) gradients are either coupled or not, make distinct predictions about east and west tropical Pacific pH values and gradients (Fig. 1). Because surface pH values are strongly linked to regional and basin-scale ocean circulation patterns, which of these states the early Pliocene to late Miocene Pacific operated under has major implications for atmospheric circulation, weather patterns and ocean productivity.

The δ^{11}B-pH proxy is based on the pH-dependent speciation of boron between two predominant aqueous species in seawater: boric acid ($B(OH)_3$) at low pH and borate ion ($B(OH)_4^-$) at high pH, with an equilibrium fractionation of ^{10}B and ^{11}B between these two species. Only the borate ion is believed to be incorporated into biogenic carbonates and thus there is a predictable relationship between the δ^{11}B of biogenic calcite (specifically, of planktonic foraminifera for the surface ocean) and ambient ocean pH[34,35]. Using boron isotopes, we here reconstruct zonal pH gradients in the tropical Pacific since the late Miocene (Fig. 2) and use a coupled ocean–atmosphere climate model to provide a mechanistic explanation for the apparent Pliocene paradox.

We analysed δ^{11}B in at least ~150 tests per sample of the mixed layer-dwelling (see Extended Data Table 1) foraminifer *Orbulina universa* from the western equatorial Pacific (WEP, Ocean Drilling Program (ODP) Site 806) and eastern equatorial Pacific (EEP, ODP Site 846) at around 1 Ma, 3 Ma and 6 Ma. Each time slice includes four samples spanning about 300 kyr (n = 24). Our strategy was designed to sample a range of orbital configurations per time slice to capture the mean and variance in conditions. Although we do not expect to capture the full extent of orbital variability in each time slice, the variation in our ~3 Ma sample is comparable to that of an orbitally resolved record over the same time span, providing support for the approach (Fig. 2). We then converted δ^{11}B values to pH using a previously published *O. universa*-specific core top calibration[36] (see Methods). In the WEP, δ^{11}B averaged 17.67‰ (~1 Ma), 16.63‰ (~3 Ma) and 16.76‰ (~6 Ma) (mean analytical uncertainty (2σ), 0.24‰), indicating a decrease in pH from an average modern value of around 8.067 (see Methods for

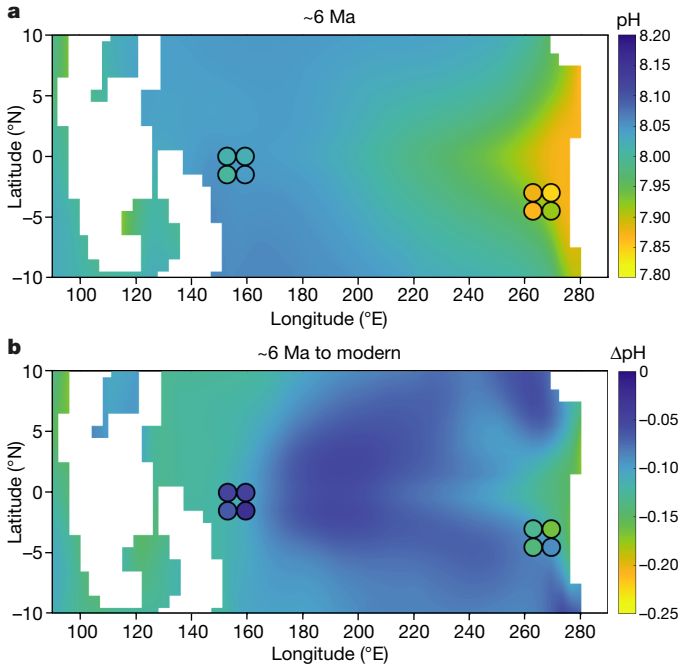

Fig. 3 | Model output shows similar results in pH and pH-anomaly relative to modern. a, Climatological pH averaged over 25–55 m depth from the last 100 years of the early Pliocene/late Miocene simulation (contours), overlaid with δ^{11}B-derived pH data (circles) from the late Miocene (~5.7, ~5.8, ~5.9 and ~6.0 Ma clockwise from top right). More acidic waters shown in yellow-green. **b**, Same as **a** but depicting the difference in the early Pliocene/late Miocene minus pre-industrial control runs of the model (more acidic waters during the early Pliocene/late Miocene shown in yellow-green). Coloured circles show anomalies from ~6.0 Ma data to average modern pH (~8.067 in the west, ~8.007 in the east).

details of observational measurements of pH) to around 8.02 in the late Miocene (~6 Ma, mean pH uncertainty (2σ) ~0.05 from Monte Carlo simulations) (Fig. 2).

Our surface pH estimates for the WEP—a region understood to be approximately in equilibrium with the atmosphere[37] through the study interval due to a weak wind field and deep thermocline—are consistent with the decline one would expect in response to current estimates of atmospheric CO_2 concentrations during each interval (see Extended Data Fig. 1).

In the EEP (ODP Site 846), pH likewise declines from ~1 Ma to ~6 Ma but at a magnitude larger than the WEP, declining from an average modern pH value of around 8.007 to around 7.88 at about 6 Ma (uncertainty (2σ), ~0.06) (Fig. 2). This results in much greater zonal pH gradients (~2–3 times greater) at around 3–6 Ma than in recent times (average modern pH gradient ~0.06). The average zonal pH gradient (Fig. 2) varies from around 0.04 to around 0.17 to around 0.14 at approximately 1 Ma, 3 Ma and 6 Ma, respectively.

This three-fold increase in the equatorial Pacific zonal pH gradient at around 3 Ma and around 6 Ma is inconsistent with an El Niño-like coupling of physical (SST) and biogeochemical (pH) gradients (Fig. 1, coupled scenarios). Rather, our reconstructed zonal pH gradient suggests changes in zonal SST and pH gradients were decoupled over this interval (Fig. 1, decoupled). New simulations using a coupled ocean–atmosphere climate model, meant to reproduce the background early Pliocene/late Miocene climate state[4,16], run for the first time with active biogeochemical cycling (the Community Earth System Model, CESM 1.0.4, see Methods), generates pH changes similar to our results (Fig. 3, Extended Data Fig. 2a). In these simulations, cloud albedo has been modified to generate an early Pliocene/late Miocene climate state with strongly reduced zonal and meridional temperature gradients in agreement with SST reconstructions[4,10,16,38–41]. While a simulation that reproduces early Pliocene/late Miocene climate without these cloud albedo modifications would be ideal, other (for example, PlioMIP2) models without these cloud albedo modifications target the mid-Pliocene warm period[26]. Future studies should therefore assess whether a simulation of early Pliocene/late Miocene climate without cloud albedo modifications and with more standard model parameters can replicate existing and our proxy data.

The modelled early Pliocene/late Miocene ocean has pH values of around 8.00–8.05 in the WEP and around 7.85–7.90 in the EEP (Fig. 3a) over a 25–55-m depth range (the approximate habitat of *O. universa*[36,42,43]), similar to our δ^{11}B-pH proxy data at ~6 Ma and, to a somewhat lesser extent, at ~3 Ma (Extended Data Fig. 2b–c). More broadly, however, model output over 25–75 m in depth generally agrees with δ^{11}B-pH proxy data (Extended Data Fig. 2a, Extended Data Fig. 2d–g). A further comparison of the experiment-minus-control model anomalies and the proxy-minus-modern anomalies is made in Fig. 3b. Both data and model output show early Pliocene/late Miocene changes relative to the modern/control of around −0.12 to −0.15 pH units in the east and relatively less pH change in the west. There is some model-data discrepancy in the magnitude of change in the west, with the model output exhibiting a slightly stronger anomaly of around −0.10 pH units relative to modern than is seen in the proxy data (around −0.05 pH units relative to modern; for further discussion see Supplementary Information). Nonetheless, the pattern in both the model output and proxy data is of increased zonal pH gradients at around 3 Ma and 6 Ma, even as zonal temperature gradients were decreased[1,3,7,8,11] (Figs. 2, 3; Extended Data Fig. 2).

The model simulations suggest that the enhanced ocean acidity in the east relative to the west can be explained by the upwelling of older waters in the east associated with a large-scale reorganization of Pacific circulation. The most dramatic changes include deep water formation in the North Pacific and an active Pacific meridional overturning circulation (PMOC)[16], both of which are absent in the Pacific Ocean today and together increase the acidity of the intermediate waters being upwelled into the eastern equatorial Pacific. The modelled maximum PMOC strength is ~15 sverdrups (1 Sv = 10^6 m^3 s^{-1}, see Fig. 4b and Extended Data Fig. 3), comparable to the modern Atlantic meridional overturning circulation (AMOC)[44].

Several features of this circulation regime contribute to the anomalously acidic water in the EEP cold tongue. First, deep water formation in the subarctic North Pacific introduces an anomalous interhemispheric gradient in mid- to deep-water pH relative to the pre-industrial ocean, with high-pH water in the Northern Hemisphere and low-pH water in the Southern Hemisphere (at the end of PMOC and AMOC flow paths) (Fig. 4a). Second, relatively more acidic (Fig. 4a) and older (Fig. 4b) water is brought up by the PMOC to intermediate depths (1,000 m) in the southern and tropical Indo-Pacific (Fig. 4c). This acidic intermediate water is then readily upwelled in the EEP because of a warm, less stratified thermocline relative to modern[5,9]. According to Fig. 4, in the presence of the PMOC roughly 4 Sv of additional water enters the subtropical overturning cells (STCs) and equatorial thermocline, shoaling from around 1,000 m depth in the Southern Hemisphere to around 200 m in the tropics. This is close to 30% of the maximum volume transport of the PMOC. Third, along the pathways taken by water subducted in the subarctic North Pacific (Fig. 4d), water parcels spend a prolonged period of time at intermediate depths—taking ~800 years to arrive at the equator after transiting along the deep limb of the PMOC, with some parcels even taking several millennia—thereby gaining nutrients and acidity before upwelling in the EEP. In the modern climate, EEP thermocline waters largely originate from water subducting in the subtropical cells and only take around 10–60 years after subduction to transit into the EEP[45].

While these results on their own cannot rule out potential effects of changes to other meridional overturning circulations (for example, the AMOC or shallow STCs) or water masses (for example, Antarctic Bottom Water, Antarctic Intermediate Water), a number of dynamical

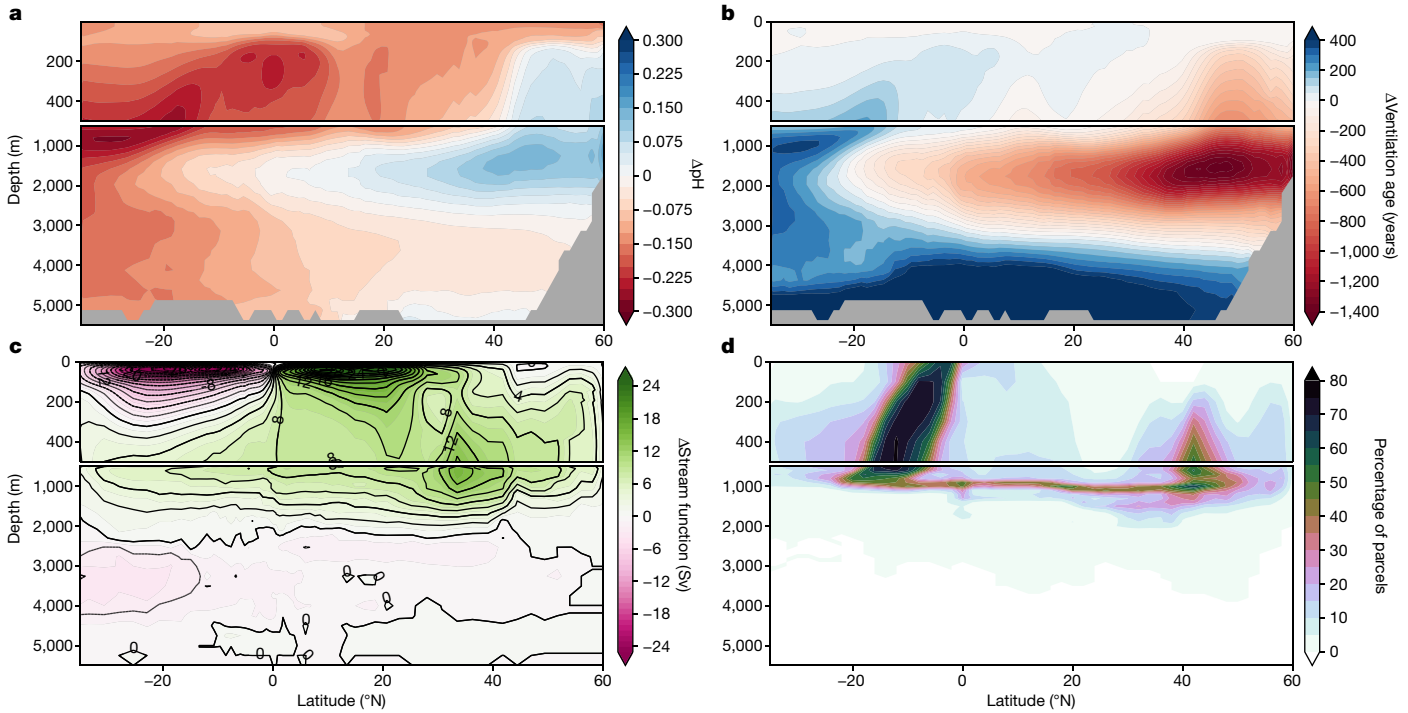

Fig. 4 | Model output (pH, ventilation age and water mass transport) evinces a Pacific meridional overturning circulation in which water parcels spend a prolonged time at depth. a–**d**, Zonally averaged meridional transects of pH anomaly (more acidic water in Pliocene in red, **a**); ventilation age anomaly (older water in Pliocene in blue, **b**); early Pliocene/late Miocene stream function (clockwise circulation in green, counterclockwise in pink, **c**); and early Pliocene/late Miocene latitude-depth water parcels pathways (**d**), depicted as percentage of parcels sourced from a North Pacific deep water formation site entering each grid cell and showing the density of parcel trajectories connecting the northern Pacific deep-water formation region with the tropical ocean. Note, all panels are zonally averaged as the overturning pathway (that is, panel **c**) spans both the western and eastern sectors of the Pacific (travelling southward along the western side of the basin, then travelling up and eastward to the surface in the EEP via the equatorial undercurrent). Panel **c** for the pre-industrial control run is reproduced in Extended Data Fig. 3e; no plot of pre-industrial pathways was produced as no such pathways as depicted in panel **d** exist in the modern Pacific.

considerations make an active PMOC a robust interpretation of this pH record (see Supplementary Information). In brief, we expect that other overturning circulations and/or water masses are unlikely to drive the observed pH patterns owing to their depths (for example, ocean abyssal cells), locations of major impacts (the AMOC), or equilibration time scales and the sign of changes (for example, STCs) (Extended Data Fig. 3).

The upwelling of old, acidic water in the east Pacific and associated delivery of more nutrients to the surface ocean contrasts with the view, based on modern observations, that nutrient delivery and productivity in warm oceans will be low, particularly in the eastern tropical Pacific, due to decreased wind-driven upwelling[46]. Our combined boron isotope data and model results (Fig. 3, Extended Data Fig. 2) show that old, more acidic, intermediate water can upwell in the EEP as a result of an active PMOC and decreased thermal stratification in the uppermost ocean. Our findings are most parsimoniously explained by more nutrient-rich water upwelling, and not greater upwelling volumes, since the STCs in the early Pliocene/late Miocene model run are clearly weaker than those in the pre-industrial control run (with northern and southern STCs of ~32 Sv and ~30 Sv respectively in the early Pliocene/late Miocene run versus ~38 Sv and ~46 Sv in the pre-industrial control run; see Extended Data Fig. 3e-h). Our results provide a dynamic mechanism for the enhanced biological productivity in the east Pacific despite warmer SSTs and a reduced zonal SST gradient during the early Pliocene to late Miocene, resolving the apparent paradox of decoupled SSTs and biological productivity.

The implications of our results for the future of the EEP depend on the timescale involved. Modelling results suggest such a more El Niño-like mean ocean state (in terms of SSTs) may take up to 100 years to develop in response to a rise in pCO_2 levels[21,47]. However, the long adjustment timescale of the deep ocean circulation implies that it would take on the order of ~1,000–1,500 years for the PMOC to develop in response to this warming (Extended Data Fig. 3c–d). In other words, the decoupling of temperature and pH gradients is predicted to develop progressively over a period of a thousand years or longer. With that in mind, increased temperatures and stratification in the EEP remain a major concern over the coming centuries given that EEP upwelling currently supports one of the most productive fisheries in the world and provides key economic and ecosystem services to local communities[48,49], services whose importance will only increase with continued population growth and development. However, given that the emissions trajectories we set today will shape the climate for millennia[50], such long-term dynamics as we've discussed here are not outside the realm of possibility either. More broadly, our results provide novel constraints on the structure and dynamics of the ocean of the early Pliocene and late Miocene by moving beyond the SST proxies typically employed and help constrain future changes in ocean dynamics as the ocean adjusts to a warming world.

Online content

Any methods, additional references, Nature Research reporting summaries, source data, extended data, supplementary information, acknowledgements, peer review information; details of author contributions and competing interests; and statements of data and code availability are available at https://doi.org/10.1038/s41586-021-03884-7.

1. Wara, M. W., Ravelo, A. C. & Delaney, M. L. Permanent El Niño-like conditions during the Pliocene warm period. *Science* **309**, 758–761 (2005).
2. Fedorov, A. V. et al. The Pliocene paradox (mechanisms for a permanent El Niño). *Science* **312**, 1485–1490 (2006).

3. Zhang, Y. G., Pagani, M. & Liu, Z. A 12-million-year temperature history of the tropical Pacific Ocean. *Science* **344**, 84–88 (2014).
4. Fedorov, A. V., Burls, N. J., Lawrence, K. T. & Peterson, L. C. Tightly linked zonal and meridional sea surface temperature gradients over the past five million years. *Nat. Geosci.* **8**, 975–980 (2015).
5. Ford, H. L., Ravelo, A. C., Dekens, P. S., LaRiviere, J. P. & Wara, M. W. The evolution of the equatorial thermocline and the early Pliocene El Padre mean state. *Geophys. Res. Lett.* **42**, 4878–4887 (2015).
6. Tierney, J. E., Haywood, A. M., Feng, R., Bhattacharya, T. & Otto-Bliesner, B. L. Pliocene warmth consistent with greenhouse gas forcing. *Geophys. Res. Lett.* **46**, 9136–9144 (2019).
7. Lawrence, K. T., Liu, Z. & Herbert, T. D. Evolution of the eastern tropical Pacific through Plio-Pleistocene glaciation. *Science* **312**, 79–83 (2006).
8. Dekens, P. S., Ravelo, A. C. & McCarthy, M. D. Warm upwelling regions in the Pliocene warm period. *Paleoceanography* **22**, PA3211 (2007).
9. Ford, H. L., Ravelo, A. C. & Hovan, S. A deep Eastern Equatorial Pacific thermocline during the early Pliocene warm period. *Earth Planet. Sci. Lett.* **355**, 152–161 (2012).
10. Fedorov, A. V. et al. Patterns and mechanisms of early Pliocene warmth. *Nature* **496**, 43–49 (2013).
11. O'Brien, C. L. et al. High sea surface temperatures in tropical warm pools during the Pliocene. *Nat. Geosci.* **7**, 606–611 (2014).
12. Ravelo, A. C., Lawrence, K. T., Fedorov, A. & Ford, H. L. Comment on "A 12-million-year temperature history of the tropical Pacific Ocean". *Science* **346**, 1467 (2014).
13. Lyle, M. Neogene carbonate burial in the Pacific Ocean. *Paleoceanography* **18**, 1059 (2003).
14. Lyle, M. & Baldauf, J. Biogenic sediment regimes in the Neogene equatorial Pacific, IODP Site U1338: burial, production, and diatom community. *Palaeogeogr. Palaeoclimatol. Palaeoecol.* **433**, 106–128 (2015).
15. Ma, Z., Ravelo, A. C., Liu, Z., Zhou, L. & Paytan, A. Export production fluctuations in the eastern equatorial Pacific during the Pliocene-Pleistocene: reconstruction using barite accumulation rates. *Paleoceanography* **30**, 1455–1469 (2015).
16. Burls, N. J. et al. Active Pacific meridional overturning circulation (PMOC) during the warm Pliocene. *Sci. Adv.* **3**, e1700156 (2017).
17. Bjerknes, J. Atmospheric teleconnections from the equatorial Pacific. *Mon. Wea. Rev* **97**, 163–172 (1969).
18. Philander, S. G. El Niño, La Niña, and the southern oscillation. *Int. Geophys. Ser.* **46**, 289 (1989).
19. Iizumi, T. et al. Impacts of El Niño SOUTHERN OSCILLATION on the global yields of major crops. *Nat. Commun.* **5**, 3712 (2014).
20. Anderson, W., Seager, R., Baethgen, W. & Cane, M. Crop production variability in North and South America forced by life-cycles of the El Niño Southern Oscillation. *Agric. For. Meteorol.* **239**, 151–165 (2017).
21. Heede, U. K., Fedorov, A. V. & Burls, N. J. Time scales and mechanisms for the tropical Pacific response to global warming: a tug of war between the ocean thermostat and weaker Walker. *J. Clim.* **33**, 6101–6118 (2020).
22. Foster, G. L., Royer, D. L. & Lunt, D. J. Future climate forcing potentially without precedent in the last 420 million years. *Nat. Commun.* **8**, 14845 (2017).
23. Haywood, A. M. et al. Large-scale features of Pliocene climate: results from the Pliocene Model Intercomparison Project. *Clim. Past* **9**, 191–209 (2013).
24. Haywood, A. M., Dowsett, H. J. & Dolan, A. M. Integrating geological archives and climate models for the mid-Pliocene warm period. *Nat. Commun.* **7**, 10646 (2016).
25. Prescott, C. L. et al. Assessing orbitally-forced interglacial climate variability during the mid-Pliocene warm period. *Earth Planet. Sci. Lett.* **400**, 261–271 (2014).
26. Haywood, A. M. et al. The Pliocene Model Intercomparison Project Phase 2: large-scale climate features and climate sensitivity. *Clim. Past* **16**, 2095–2123 (2020).
27. Brierley, C. M. & Fedorov, A. V. Relative importance of meridional and zonal sea surface temperature gradients for the onset of the ice ages and Pliocene-Pleistocene climate evolution. *Paleoceanography* **25**, PA2214 (2010).
28. McClymont, E. L. et al. Lessons from a high-CO_2 world: an ocean view from ~3 million years ago. *Clim. Past* **16**, 1599–1615 (2020).
29. Burls, N. J. et al. Simulating Miocene warmth: insights from an opportunistic multi-model ensemble (MioMIP1). *Paleoceanogr. Paleoclimatology* **36**, e2020PA004054 (2021).
30. Ravelo, A. C., Dekens, P. S. & McCarthy, M. Evidence for El Niño-like conditions during the Pliocene. *GSA Today* **16**, 4–11 (2006).
31. Liu, J. et al. Eastern equatorial Pacific cold tongue evolution since the late Miocene linked to extratropical climate. *Sci. Adv.* **5**, eaau6060 (2019).
32. Wycech, J. B., Gill, E., Rajagopalan, B., Marchitto, T. M. Jr & Molnar, P. H. Multiproxy reduced-dimension reconstruction of Pliocene equatorial Pacific sea surface temperatures. *Paleoceanogr. Paleoclimatology* **35**, e2019PA003685 (2020).
33. White, S. M. & Ravelo, A. C. The benthic B/Ca record at Site 806: new constraints on the temperature of the West Pacific Warm Pool and the "El Padre" state in the Pliocene. *Paleoceanogr. Paleoclimatology* **35**, e2019PA003812 (2020).
34. Rae, J. W. B., Foster, G. L., Schmidt, D. N. & Elliott, T. Boron isotopes and B/Ca in benthic foraminifera: proxies for the deep ocean carbonate system. *Earth Planet. Sci. Lett.* **302**, 403–413 (2011).
35. Rae, J. W. B. in *Boron Isotopes* (eds. Marschall, H. & Foster, G.) 107–143 (Springer, 2018).
36. Henehan, M. J. et al. A new boron isotope-pH calibration for Orbulina universa, with implications for understanding and accounting for 'vital effects'. *Earth Planet. Sci. Lett.* **454**, 282–292 (2016).
37. Takahashi, T. et al. Climatological mean and decadal change in surface ocean pCO_2, and net sea–air CO_2 flux over the global oceans. *Deep Sea Res. Part II Top. Stud. Oceanogr.* **56**, 554–577 (2009).
38. Burls, N. J. & Fedorov, A. V. Simulating Pliocene warmth and a permanent El Niño-like state: the role of cloud albedo. *Paleoceanography* **29**, 893–910 (2014).
39. Burls, N. J. & Fedorov, A. V. What controls the mean east–west sea surface temperature gradient in the equatorial Pacific: the role of cloud albedo. *J. Clim.* **27**, 2757–2778 (2014).
40. Dowsett, H. J. et al. Sea surface temperature of the mid-Piacenzian ocean: a data-model comparison. *Sci. Rep.* **3**, 2013 (2013).
41. Brierley, C., Burls, N., Ravelo, C. & Fedorov, A. Pliocene warmth and gradients. *Nat. Geosci.* **8**, 419–420 (2015).
42. Sautter, L. R. & Thunell, R. C. Planktonic foraminiferal response to upwelling and seasonal hydrographic conditions; sediment trap results from San Pedro Basin, Southern California Bight. *J. Foraminifer. Res.* **21**, 347–363 (1991).
43. Rebotim, A. et al. Factors controlling the depth habitat of planktonic foraminifera in the subtropical eastern North Atlantic. *Biogeosciences* **14**, 827–859 (2017).
44. Buckley, M. W. & Marshall, J. Observations, inferences, and mechanisms of the Atlantic Meridional Overturning Circulation: a review. *Rev. Geophys.* **54**, 5–63 (2016).
45. Thomas, M. D. & Fedorov, A. V. The eastern subtropical Pacific origin of the equatorial cold bias in climate models: a Lagrangian perspective. *J. Clim.* **30**, 5885–5900 (2017).
46. Sarmiento, J. L., Hughes, T. M. C., Stouffer, R. J. & Manabe, S. Simulated response of the ocean carbon cycle to anthropogenic climate warming. *Nature* **393**, 245–249 (1998).
47. Fedorov, A. V., Brierley, C. M. & Emanuel, K. Tropical cyclones and permanent El Niño in the early Pliocene epoch. *Nature* **463**, 1066–1070 (2010).
48. Christensen, V., De la Puente, S., Sueiro, J. C., Steenbeek, J. & Majluf, P. Valuing seafood: the Peruvian fisheries sector. *Mar. Policy* **44**, 302–311 (2014).
49. Gutierrez, D., Akester, M. & Naranjo, L. Productivity and sustainable management of the Humboldt Current large marine ecosystem under climate change. *Environ. Dev.* **17**, 126–144 (2016).
50. Clark, P. U. et al. Consequences of twenty-first-century policy for multi-millennial climate and sea-level change. *Nat. Clim. Chang.* **6**, 360–369 (2016).
51. Martínez-Botí, M. A. et al. Plio-Pleistocene climate sensitivity evaluated using high-resolution CO_2 records. *Nature* **518**, 49–54 (2015).

Publisher's note Springer Nature remains neutral with regard to jurisdictional claims in published maps and institutional affiliations.

© The Author(s), under exclusive licence to Springer Nature Limited 2021

Methods

Study sites and species selection

To reconstruct the zonal pH gradient across the equatorial Pacific since the late Miocene, samples were taken at ~1 Ma, ~3 Ma and ~6 Ma from two sites in the eastern and western equatorial Pacific. The eastern site, ODP Site 846 (3° 5.7′S, 90° 49.1′W, water depth ~3,300 m), is located approximately 300 km south of the Galapagos Islands near the convergence of the South Equatorial Current (SEC) and Peru Current and sits atop the Carnegie Ridge[52]. It sits in the central region of the east Pacific cold tongue and is subject to strong upwelling of deep water. The western site, ODP Site 806 (0° 19.1′N, 159° 21.7′E, water depth ~2,500 m) is located ~700 km west of Papua New Guinea on the Ontong Java Plateau[53]. It is situated in the heart of the west Pacific warm pool, a region in equilibrium with the atmosphere with respect to CO_2 (ref. [37]). Both sites exhibit moderate to moderate-to-good preservation of planktonic foraminifera through to the late Miocene[52,53] . Importantly, $\delta^{11}B$ measurements have been demonstrated to be relatively insensitive to dissolution, with several studies showing close agreement of $\delta^{11}B$ between time-equivalent samples at sites of different carbonate preservation and burial histories[54–56] (except, see Hönisch and Hemming[57]). In the authoritative paper on this subject, Edgar et al. compared samples of planktonic foraminifera from two sites of similar paleoceanographic settings but vastly different carbonate preservation states (the clay-rich TDP Site 18 in the Indian Ocean and the carbonate-rich ODP Site 865 in the central Pacific Ocean) and found no significant difference in $\delta^{11}B$ recorded at the two sites, despite extensive dissolution in the ODP 865 samples[54]. Furthermore, a categorical offset found in other geochemical tracers (for exanple, $\delta^{18}O$, $\delta^{13}C$, Sr/Ca and B/Ca) but no offset in $\delta^{11}B$ gave further evidence of $\delta^{11}B$ being uniquely robust to dissolution effects. Based on this evidence, our samples should be robust to dissolution effects with regard to $\delta^{11}B$, even in samples of moderate preservation.

These sites have been the focus of numerous previous studies of the Pacific zonal SST gradient during the Pliocene[1–3,6–9,11,30,32,33,58]. A broad synthesis of this data and model simulations is presented by Fedorov et al.[4,10] as well as McClymont et al.[28]. While several studies have sampled from ODP Site 847 in the east Pacific[1,8,11,30], we have elected to use samples from ODP Site 846 since this site, being slightly south of the equator, is likely to be less affected by the formation of the Galapagos archipelago ~1.6 Mya (ref. [59]). Samples were taken from between 36 and 232 m composite depth (mcd) at ODP Site 846 and between 8 and 177 mcd at ODP Site 806.

The LR04 age model[60] was used for the eastern ODP Site 846, while the western ODP Site 806 use the age model of Zhang et al.[61], updated to the GTS 2004 timescale[62]. The planktonic foraminifera *Trilobatus sacculifer* (formerly *Globigerinoides sacculifer*[63] and the focal species in previous studies of the Pliocene equatorial Pacific[1]) was not abundant enough in samples from ODP Site 846 for boron isotope analysis; sample assemblages were dominated by radiolarians with foraminifera making up only a small portion of the coarse fraction material. *Orbulina universa* was abundant enough, however, at both sites in the 300–355 mm size fraction to pick the ~150–200 individuals needed for each $\delta^{11}B$ measurement. Like *T. sacculifer*, *O. universa* makes its habitat in the mixed layer (~25–50 m) where waters are well mixed and in communication with the atmosphere and has been calibrated for boron isotopes[36], making it a suitable candidate for this study of mixed layer pH[36,42,43].

Our sampling strategy aimed to reconstruct the evolution of the zonal Pacific pH gradient since the latest Miocene. Samples were taken at three large time steps (~1 Ma, ~3 Ma and ~6 Ma) with four more closely spaced samples within each of these windows (every ~100 ka) to capture some extent of orbital variability. Our samples at ~1 Ma, for example, all fall within different stages of the glacial-interglacial cycles of the Pleistocene (Extended Data Fig. 4a, b). A more thorough treatment of glacial–interglacial pH changes is performed in other studies, particularly in Martínez-Botí and colleagues[64]. At a site in equilibrium with the atmosphere similar to our WEP site (PS2498-1 in the south central Atlantic), pH had a maximum range of 0.14 over the record (from ~2.24–15.90 ka) with ~95% of that variation (2σ) varying within just 0.06, for an average glacial-interglacial (~2.24–10.28 ka versus ~15.12–15.90 ka) pH change of 0.09. The EEP site ODP 1238 in ref. [64] has a maximum range and 2σ of 0.23 and 0.13 over the record (~1.03–20.60 ka). For comparison, our data at ~1 Ma (the time slice with the lowest within-site variance) has pH ranges of 0.05 and 0.06 for the WEP and EEP, respectively, suggesting—by comparison to ref. [64]—that we may not capture the full glacial–interglacial range in pH at 1 Ma. However, this does not affect the main finding of our study—that the zonal equatorial Pacific pH gradient in the early Pliocene/late Miocene (~0.17 and ~0.14 at ~3 Ma and ~6Ma, respectively) was enhanced relative to modern (~0.06)—given that the zonal gradients are roughly constant over the full glacial–interglacial cycle (for example, 0.08 in the glacial and 0.05 in the interglacial as calculated from ref. [64]). Additionally, each of our samples are likely to integrate over ~10,000 years, minimizing concerns about mismatched time intervals captured by samples from the eastern and western Pacific sites (see also Extended Data Fig. 4).

Estimation of modern pH

To constrain modern values for eastern and western equatorial Pacific pH, we compiled observational measurements from all available cruise data near our sites from the past several decades to estimate the possible domain of modern variability in pH.

We have compiled direct measurements of pH (or occasionally, alkalinity and total dissolved inorganic carbon (DIC), from which pH may be calculated) from every cruise passing within 5° of latitude and longitude of our study sites, as available from the GLODAPv1[65] and v2[66], PACIFICA[67] and WOCE[68] databases (18 cruises from 1992–2018, with 16 cruises in the west Pacific and two cruises in the east, not counting the eastern La Niña-year cruise, which was not taken near our study site (~20° west of it) so was only included for illustrative purposes and not included in any further analysis). Each cruise made multiple depth-profile measurements of either pH or alkalinity and DIC (68 profiles in total), which have been compiled into Extended Data Fig. 5. Where direct measurements of pH were not available, pH was calculated from alkalinity and DIC within Ocean Data View[69] using the *Best Practices* handbook[70] equilibrium constants, which give results in excellent agreement with other carbonate system calculations (for example, CO_2SYS (ref. [71])). The El Niño conditions under which each profile was taken was determined from the Oceanic Niño Index (ONI) product reported by NOAA's Climate Prediction Center[72,73].

Estimates of modern pH in the eastern and western equatorial Pacific were derived only from neutral ENSO years (Extended Data Fig. 5a, with 12 profiles from one cruise in the east and 21 profiles from five cruises in the west, which were linearly interpolated onto uniform 1 m depth intervals and averaged together (Extended Data Fig. 5d). These average depth profiles were then averaged over the 25–50 m depth range (the approximate depth habitat of *O. universa*; see Supplementary Information and Extended Data Table 1) to produce estimates of modern pH against which to compare our proxy data (8.007 ± 0.062 and 8.067 ± 0.007 for the east and west, respectively (1σ)). An interesting observation from this pH compilation is that the zonal pH gradient is less pronounced at the surface than it is a few tens of metres deeper, making our choice to use *O. universa* more appropriate for detecting such signals in the past than, say, a shallower-dwelling species such as *T. sacculifer*.

More empirical data are needed from the eastern Pacific, and we therefore hesitate to put too much emphasis on data from a limited number of observations. For example, rather than the collapse of the zonal pH gradient expected during an El Niño event with its reduced upwelling, the pH gradient over 25–50 m depth that we find under El Niño conditions (~0.09, Extended Data Fig. 5b) is slightly greater but

within variability of the average gradient found under neutral ENSO conditions (~0.06, Extended Data Fig. 5a). However, we do find an enhanced zonal pH gradient under La Niña conditions (~0.12, Extended Data Fig. 5c), consistent with increased east Pacific upwelling in a La Niña event (although note that the EEP cruise used to get this number was from a site ~20° west of our study site so is not directly comparable). Notably, we record in our proxy data zonal pH gradients even greater than this at ~3 Ma (~0.17 on average) and ~6 Ma (~0.14 on average).

Without more data available, the best practice is to constrain the possible domain of modern variability as we have done here. Accordingly, we have included in Fig. 2 both the average and 1σ of the 25–50 m averaged pH from all neutral-year profiles compiled from the east (blue diamond with error bars) and west (red diamond with error bars) Pacific. We have also reproduced Fig. 2 with every neutral-year profile's 25–50 m average pH being shown as dashes along its *y* axis (Extended Data Fig. 6).

Hypothesis figure

The schematic of Fig. 1 was generated by applying the same proportional reduction in the zonal thermal (SST) gradient (in the early Pliocene/late Miocene relative to modern) as found by different studies to the modern-day zonal pH gradient. First, modern WEP and EEP pH was found as described in the 'Estimation of modern pH' section, providing the anchor points on the left-hand side of the plot. Next, a representative early Pliocene/late Miocene WEP pH (~8.02) was estimated from an equilibrium state with 400 ppm atmospheric CO_2 and a modern-like alkalinity (2,275 µmol kg^{-1}) (alkalinity is understood to have been relatively invariant over the Cenozoic, staying close to modern values[74]). Finally, for the dotted and dashed blue lines, an early Pliocene/late Miocene EEP pH was estimated from the reported reductions in the late Miocene zonal thermal (SST) gradient relative to modern as found by Liu et al.[31] (dotted line, an ~82% reduction) and Zhang et al.[3] (dashed line, a ~28% reduction). The percent-reduction in the zonal thermal gradient relative to modern as found by each of those studies was then applied to the magnitude of the modern zonal pH gradient (~0.06), resulting in a representative early Pliocene/late Miocene zonal pH gradient of either 0.017 (dotted line)[31] or 0.049 (dashed line)[3]. Early Pliocene/late Miocene EEP pH was estimated by applying those pH gradients to the early Pliocene/late Miocene WEP pH estimate (~8.02), resulting in early Pliocene/late Miocene EEP pH values of ~8.003 (dotted) and ~7.971 (dashed). The solid blue line depicts the EEP average pH put out by the coupled ocean–atmosphere climate model used in this study in its early Pliocene/late Miocene-like run over the 25–55 m depth range (~7.886), which is interpreted to reflect a decoupling between early Pliocene/late Miocene zonal thermal and pH gradients. The model could not be averaged down to 50 m exactly as its depth intervals went in steps of 10 m (that is, 25 m, 35 m, 45 m, 55 m).

Sample preparation for boron isotope and trace elements analysis

Initial preparation of marine sediment samples involved disaggregating samples in sodium hexametaphosphate solution (2 g l^{-1}) buffered with ammonium hydroxide (NH_4OH), washing in deionized water over a 64 µm sieve, and drying in a <50 °C oven. Samples were rewashed until visually clean. Individuals of *O. universa* were picked from the 300–355 µm size range. Occasionally individuals from other size fractions were included (down to 250 µm and up to 710 µm, but rarely outside of the 300–600 µm range) if foraminifera were sparse, as the boron-pH calibration for *O. universa* has no statistically significant size trend within this range[36]. Sample sizes typically range from ~150–200 foraminifera and ~2–4 mg of $CaCO_3$.

All subsequent laboratory procedures were carried out in a Picotrace class ten clean lab at the Yale Metal Geochemistry Center (Yale University) in an over-pressurized hood equipped with boron-free filters and using Milli-Q water (18.2 MΩ with Q-Gard boron removal pack) and Teflon-distilled nitric acid (HNO_3). Approximately ~2.5 mg of solid carbonate sample (that is, the picked *O. universa*) was cleaned following the procedure outlined in Foster et al.[75] and Rae et al.[34], and references therein. After lightly cracking open individual chambers between clean glass slides, the solid sample was repeatedly ultrasonicated and rinsed with Milli-Q water (5 × 30 s of ultrasonication) to remove clays. Organic matter was removed by subjecting the solid to oxidative cleaning using 250 µl of 1% hydrogen peroxide (H_2O_2) in 0.1 M NH_4OH at 80 °C for 3 × 5 min, with 15 s of ultrasonication in between. Afterwards, 250 µl of 0.0005 M HNO_3 was added to the solid for 30 s as a brief weak acid leach to remove any re-adsorbed contaminants. Samples were then rinsed twice with Milli-Q water. Finally, samples had 200 µl of Milli-Q water added to them before incrementally adding 0.5 M HNO_3 acid until the sample was totally dissolved (anywhere from 75 to 200 µl). The sample was centrifuged for 5 min to isolate any undissolved contaminant phases. A small aliquot (approximately 7% of the volume) of the supernatant was transferred to an acid-cleaned plastic centrifuge tube for trace metal analysis, and the remaining supernatant was transferred to a Teflon beaker for isotope analysis.

Boron was separated from the dissolved carbonate matrix by passing the sample through pre-cleaned heat-shrunk Teflon micro-columns containing 20 µl of ground, sieved (63–100 µm) boron-specific anionic exchange resin (Amberlite IRA 743[76]) following the procedure of Foster and colleagues[75]. Before performing column chemistry, the columns were cleaned by passing a full-column's volume of 0.5 M HNO_3 plus 1 ml of 0.5 M HNO_3 plus 2 × 1 ml of Milli-Q through each of the columns. Samples were also buffered prior to column chemistry with boron-clean sodium acetate buffer (twice the volume of acid required to dissolve the solid sample) to maintain sample pH > 5. The sample matrix was then rinsed through the columns by the addition of 10 × 160 µl of Milli-Q water before being eluted with 5 × 120 µl of 0.5 M HNO_3 and collected in acid-cleaned Teflon beakers. Sample tails were also collected in separate Teflon beakers with a final elution of 1 × 120 µl of 0.5 M HNO_3. Each batch of columns included a JCp-1 carbonate geostandard (Japanese Geological Survey Porites Coral[77]) to monitor column performance and reproducibility, as well as a total procedural blank (TPB) composed of 0.5 M HNO_3 and buffer to monitor cleanliness and potential sample contamination. The average blank contribution from the total procedural blank (TPB) included in each batch of columns was ~19 pg (~0.15% of average sample size).

Boron isotope analysis by MC-ICP-MS

Boron isotope analysis was performed at the Yale Metal Geochemistry Center on a Thermo Finnigan Neptune Plus MC-ICP-MS equipped with 10^{12} Ω resistors and tuned before analysis to optimize maximum $^{11}B/^{10}B$ stability, following the procedure described of Foster et al.[75] and references therein. A Teflon barrel spray chamber and ammonia gas were used for boron washout[78].

Prior to analysis, boron concentration and potential contamination by the Na-rich buffer were checked in tails an in 20 µl aliquots of samples diluted with 100 µl of 0.5 M HNO_3. Tails typically made up <1% of the boron loaded. Depending on the sample size, boron isotope samples range from ~5–13 ng, yielding solutions for analysis of ~8–21 ppb (ng g^{-1}).

Samples were bracketed with 50 ppb NIST SRM 951 boric acid standard, which was used to correct for machine-induced mass-fractionation and convert $^{11}B/^{10}B$ ratios to delta notation. To monitor accumulating blank contamination from the laboratory atmosphere while the vials were open for analysis, a blank consisting of the same volume of 0.5 M HNO_3 as the samples (600 µl) was analysed every third sample and used to correct sample $\delta^{11}B$ values. Samples were measured in duplicate, with the mean $\delta^{11}B$ being reported.

The average blank contribution from the total procedural blank (TPB) included in each batch of columns was ~19 pg (~0.15% of average sample size). Sample $\delta^{11}B$ values were corrected using TPB $\delta^{11}B$ values. The average blank correction ($\delta^{11}B_{original} - \delta^{11}B_{corrected}$) was ~0.011‰ and therefore below typical measurement uncertainty.

The uncertainty of boron isotope measurements (2σ was typically 0.24‰) was determined from a relationship between signal size and external reproducibility:

$$2\sigma = 8.67 \times \exp(-42.21[^{11}B]) + 0.25 \times \exp(-0.21[^{11}B]) \quad (1)$$

where $[^{11}B]$ is the ^{11}B signal intensity in volts. This relationship is derived from repeat analysis of multiple batches of roughly mass-matched JCp-1 pass through columns with individual sample batches. For this study, the average $\delta^{11}B$ value of JCp-1 was 24.18 ± 0.23‰ (2σ) ($n = 8$).

Trace element analysis by ICP-MS

Trace element analysis was performed at the Yale Metal Geochemistry Center on a Thermo Finnigan Element XR ICP-MS, again using a Teflon barrel spray chamber and ammonia gas and following the procedure outlined in Foster et al.[75] and references therein. In-house consistency standards (SMEG) were analysed to monitor machine behaviour. Sample matrix was matched to the [Ca] of bracketing standards to optimize reproducibility and analysed for Mg/Ca values.

Calculation of Mg/Ca SSTs

Planktonic foraminiferal Mg/Ca was measured on an aliquot of each $\delta^{11}B$ sample and used to estimate SSTs in order to accurately calculate pH from $\delta^{11}B$. Given the residence times of magnesium (~13 Myr)[79] and calcium (~1 Myr)[80] in seawater, the Mg/Ca composition of seawater (Mg/Ca_{SW}) is likely to have varied on timescales of ~1–10 Myr. We therefore account for secular change in Mg/Ca_{SW} using the Mg/Ca_{SW} record of Fantle and DePaolo[81], based on the Mg concentration of pore fluid and which closely matches estimates for the Pliocene from halite fluid inclusions[82,83]. In using this Mg/Ca_{SW} record, we follow the example of other boron-based studies of the Plio-Pleistocene[51,84]. Similarly, the Mg/Ca_{SW} record of Horita et al.[83], which closely matches the record of Fantle and DePaolo[81], has been used in a number of previous boron-based studies set in the Miocene[55,85,86].

We do not, however, account for the non-linear response of foraminiferal Mg/Ca to changing Mg/Ca_{SW} outlined by Evans and Müller, 2012[87], who show that $\frac{Mg}{Ca}_{test} \propto \left(\frac{\frac{Mg^{t=t}}{Ca_{SW}}}{\frac{Mg^{t=0}}{Ca_{SW}}}\right)^{H}$ where $0 < H < 1$ and '$t = 0$' refers to modern Mg/Ca_{SW} (5.2 mol mol^{-1})[74] and '$t = t$' refers to Mg/Ca_{SW} at different points in Earth's past, because a coefficient of non-linearity (H in Evans and Müller[87]) has not yet been calibrated for *O. universa*. While this results in lower SSTs than had the power-law relationship been assumed or the new Bayesian calibration of Tierney et al.[88] been employed (Extended Data Fig. 7a–c), we demonstrate in Extended Data Fig. 7d–f (and Extended Data Fig. 6b–c) that this does not greatly affect the pH values or conclusions of this study.

In the main text figures and analyses, SSTs are calculated from planktonic foraminiferal Mg/Ca using the *O. universa* species-specific calibration of Anand et al.[89] ($A = 0.090$, $B = 0.595$ for $Mg/Ca = B \times \exp^{AT}$), correcting for Mg/Ca_{SW} using the record of Fantle and DePaolo[81], and assuming a linear relationship between Mg/Ca_{test} and Mg/Ca_{SW} (that is, $H = 1 \text{ in } \frac{Mg}{Ca}_{test} = \left(\frac{\frac{Mg^{t=t}}{Ca_{SW}}}{\frac{Mg^{t=0}}{Ca_{SW}}}\right)^{H} B \times \exp^{AT}$).

pH and pCO_2 estimates from boron isotopes

Calculation of pH from $\delta^{11}B$ was performed using the *O. universa* calibration of Henehan et al.[36], which shows good agreement with in situ pH in core tops from numerous geographically widespread sites covering a diverse range of oceanographic environments and ambient pH and $\delta^{11}B$ of borate (Extended Data Fig. 4c). A Monte Carlo simulation was used to estimate uncertainty, following the example of numerous previous boron-pH studies[51,55,64,84,90] and using previously published code[35]. Reported pH values are the mean of 10,000 replicates of a simulation in which sea surface temperature, sea surface salinity (SSS), $\delta^{11}B_{calcite}$ and $\delta^{11}B_{SW}$, and alkalinity (for the purposes of calculating pCO_2) are randomly generated from within a frequency distribution spanning the uncertainty surrounding each parameter. Following the example of Chalk et al.[84], we place normal distributions around SST, SSS, $\delta^{11}B_{calcite}$ and $\delta^{11}B_{SW}$ and a uniform distribution spanning a generous range (±200 µmol kg^{-1}) around alkalinity.

SSTs fed into the Monte Carlo simulations were derived from Mg/Ca data described in the 'Calculation of Mg/Ca SSTs' section and, unlike other proxy data, a wider and more conservative range of uncertainty of ±2 °C is applied instead of the root sum of squares of the analytical and calibration uncertainty (which was small, less than around 0.9 °C). Uncertainty around $\delta^{11}B_{calcite}$ is the reported analytical uncertainty (2σ). Because the residence time of boron in seawater is believed to be on the order of 10–20 Myr (refs. [91–93]), the modern-day value of $\delta^{11}B_{SW}$ with its reported uncertainty (39.61 ± 0.04‰ (2σ)) is used here[94]. A generous range of sea surface salinity around a representative modern-day value is applied: 34.5 ± 1 psu. Reported uncertainty on pH is two standard deviations of the 10,000 simulated pH values. For the purpose of calculating pCO_2 estimates from the pH values, a modern-like value of alkalinity (2,275 µmol kg^{-1}) was applied with a generous range of uncertainty (±200 µmol kg^{-1}). Alkalinity is understood to have remained relatively constant over the Cenozoic[74], making this a more robust assumption (but assuming a modern-like calcite saturation state gives similar results, Extended Data Fig. 1b). Finally, a map of modern pH (Extended Data Fig. 5e–g) is provided to show the locations of our study sites versus that of the other $\delta^{11}B$-derived pH data[51] in Fig. 2.

Physical and biogeochemical modelling

Numerical simulations were performed using the National Center for Atmospheric Research (NCAR)'s coupled ocean-atmosphere Community Earth System Model (CESM) version 1.2.2, with the T31 gx3v7 configuration designed for long-term paleoclimate simulations[95]. The atmospheric and land surface components (the Community Atmosphere Model 4 and Community Land Model 4) have a spectral truncation of T31, and the oceanic and sea ice components (POP2 and Community Ice Code) have a resolution ranging from 3° near the poles to 1° at the equator. Two simulations have been performed—a pre-industrial control simulation and an early Pliocene/late Miocene-like experiment that reproduces the magnitude and spatial structure of the large-scale warming patterns, specifically the reduction in the meridional and zonal gradients seen in Pliocene SST reconstructions[4,10,40,41].

Both the control and early Pliocene/late Miocene-like experiment have the biogeochemical model enabled[96], allowing us to evaluate the impact of the simulated changes in ocean temperature, salinity and circulation on ocean pH. The simulations have been run for 3,000 years, allowing the system to reach quasi-equilibrium (Extended Data Fig. 3a–d). The analysis presented here is based on the climatology of the last 100 years of each simulation (years 2901–3000), and Pliocene/late Miocene anomalies are reported relative the pre-industrial control run.

The experimental design for the early Pliocene/late Miocene-like experiment is the same as the Early Pliocene-like simulation evaluated in Burls et al.[16] and Burls et al.[38,39] but with an active biogeochemical component. For full details, see Supplementary Information and Burls and colleagues[38,39]. In brief, mean cloud albedo is reduced in the extratropics and increased in the tropics by altering the liquid and ice water path in the shortwave radiation scheme in different latitudinal bands. The liquid water path of a cloud when it forms in the model is reduced poleward of 15°N and 15°S by 60%, while the ice and liquid water paths are increased equatorward of 15°N and 15°S by 240%. The cloud radiative forcing changes that arise due to the imposed water and ice path modifications result in a decrease in extratropical (8–90°N and 8–90°S) albedo of 0.04 and an increase in tropical albedo (8°S–8°N) of 0.06. This cloud albedo modification serves to compensate for under-represented cloud radiative effects from either poorly resolved cloud feedbacks

(strongly positive in the extratropics and negative in the deep tropics; for example, refs. [97–101]) or missing aerosol cloud indirect effects for example, Sagoo and Storelvmo[102].

All other boundary conditions (for example, the continental boundaries) and radiative forcings in the Pliocene/late Miocene-like experiment are the same as the pre-industrial control, that is, the default for the B_1850_BGC-BDRD CESM component set run on the T31_g37 grid[95]. The atmosphere, ocean, sea ice and land component of the climate system all freely evolve in response to the imposed changes in cloud shortwave radiative forcing reaching a near-equilibrium warming pattern that resembles early Pliocene and late Miocene SSTs. Note that atmospheric CO_2 was left at the pre-industrial value of 284.7 ppm in the atmospheric component and the global warming seen in this simulation is instead supported by the cloud albedo changes and the associated feedbacks, for example, the water vapour feedback (in reality elevated Pliocene CO_2 concentrations were likely to be the primary forcing responsible for the Pliocene warmth with the cloud radiative forcing changes resulting as a feedback, or due to different Pliocene aerosol concentrations). Atmospheric CO_2 was set to 400 ppm in the ocean biogeochemistry (BGC) component to correctly simulate the implications of elevated Pliocene CO_2 concentrations on ocean biogeochemistry and pH.

Lagrangian analysis of water parcel trajectories

In this study we used the Lagrangian analysis of water parcel trajectories of Thomas and colleagues[103]. Water parcel trajectories were modelled to identify the subsurface pathways taken by the PMOC water. This involved identifying both the surface source regions of deep-water formation in the North Pacific and the mixed layer destinations where that water resurfaces, and tracing the pathways between them, determined according to a Lagrangian ocean analysis approach that tracks water parcels in the Pacific Ocean of the CESM climate model (see the 'Physical and biogeochemical modelling' sectionabove for model description). This analysis was performed using the Ariane software package[104], which models water parcel trajectories by time-integrating velocity fields output by the ocean model. Trajectories calculated from ocean model momentum equations in this way—when coupled with a parameterization for subgrid-scale eddy-induced velocities (EIVs)[105]—depict the purely advective pathways of water parcels/tracers (that is, without the effect of diffusion). To resolve the long residence timescales of PMOC water in the deep ocean, particles were allowed to loop continuously over the 100 years of model output (see van Sebille et al. [106] for a discussion on particle looping).

Model tracer particles were seeded in every grid cell of the Pacific Ocean basin at 25°N and at every timestep (~1 million particles) before being integrated both backwards in time (to identify the particle mixed layer source regions at high northern latitudes) and forwards in time (to identify their mixed layer destinations). Time-integration in both cases was stopped when particles reached the model mixed layer. Particles found to originate close to the northern margin of the Pacific Ocean basin (north of ~40°N), clearly identifiable as PMOC water that is separate from the subtropical sources of the shallow wind-driven cells, were then isolated and subsequently run forwards in time from their original starting positions at 25°N. Of these, the particles that upwelled into the tropical Pacific (approximately 15% of them) were then further identified and their pathways and timescales analysed. A random subset of 12,000 particles (a number manageable within computer memory limitations) was then selected to identify the pathways taken between the sources and tropical sinks of PMOC water (Fig. 4c).

Because the CESM ocean model used in this study is configured on an Arakawa B-grid, ocean model velocities had to first be linearly interpolated onto a C-grid configuration[107] to be compatible with the Ariane software. EIV values also had to be set to zero at the ocean boundary to prevent unrealistic propagation of particles; however, the Pacific Ocean domain was found to be minimally affected by this problem, and results overall were only weakly sensitive to it.

Data availability

The proxy data and model output produced in this study are available as .xlsm and .nc files in NOAA's paleoclimate data repository (https://www.ncdc.noaa.gov/paleo/study/33252) (https://doi.org/10.25921/AMPV-J413). Source data are provided with this paper.

Code availability

The code used in this paper to produce pH from $d^{11}B$ (and to produce all the proxy-related figures) is publicly available as Matlab scripts on GitHub (https://github.com/Maddie-Sh/ShankleEtAl2021_Pliocene-pH). The CESM 1.2.2.1 code is available from https://svn-ccsm-models.cgd.ucar.edu/cesm1/release_tags/cesm1_2_2_1. The Python code used to create select model figures is available at https://github.com/nburls/ShankleEtAl2021. Source data are provided with this paper.

52. Mayer, L. A. et al. *Proceedings of the Ocean Drilling Program: Initial Report*s Vol. 138 (Ocean Drilling Program, 1992).
53. Kroenke, L. W. et al. *Proceedings of the Ocean Drilling Program: Initial Reports* Vol. 130 (Ocean Drilling Program, 1991).
54. Edgar, K. M., Anagnostou, E., Pearson, P. N. & Foster, G. L. Assessing the impact of diagenesis on $\delta^{11}B$, $\delta^{13}C$, $\delta^{18}O$, Sr/Ca and B/Ca values in fossil planktic foraminiferal calcite. *Geochim. Cosmochim. Acta* **166**, 189–209 (2015).
55. Foster, G. L., Lear, C. H. & Rae, J. W. B. The evolution of pCO_2, ice volume and climate during the middle Miocene. *Earth Planet. Sci. Lett.* **341**, 243–254 (2012).
56. Penman, D. E., Hönisch, B., Zeebe, R. E., Thomas, E. & Zachos, J. C. Rapid and sustained surface ocean acidification during the Paleocene-Eocene thermal maximum. *Paleoceanography* **29**, 357–369 (2014).
57. Hönisch, B. & Hemming, N. G. Ground-truthing the boron isotope-paleo-pH proxy in planktonic foraminifera shells: partial dissolution and shell size effects. *Paleoceanography* **19**, PA4010 (2004).
58. Chaisson, W. P. & Ravelo, A. C. Pliocene development of the east-west hydrographic gradient in the equatorial Pacific. *Paleoceanography* **15**, 497–505 (2000).
59. Karnauskas, K. B., Mittelstaedt, E. & Murtugudde, R. Paleoceanography of the eastern equatorial Pacific over the past 4 million years and the geologic origins of modern Galapagos upwelling. *Earth Planet. Sci. Lett.* **460**, 22–28 (2017).
60. Lisiecki, L. E. & Raymo, M. E. A Pliocene-Pleistocene stack of 57 globally distributed benthic $\delta^{18}O$ records. *Paleoceanography* **20**, (2005).
61. Zhang, Y. G., Pagani, M., Henderiks, J. & Ren, H. A long history of equatorial deep-water upwelling in the Pacific Ocean. *Earth Planet. Sci. Lett.* **467**, 1–9 (2017).
62. Ogg, J. G., Gradstein, F. M. & Smith, A. G. (eds.) *A Geologic Time Scale 2004* (Cambridge Univ. Press, 2004).
63. Spezzaferri, S. et al. Fossil and genetic evidence for the polyphyletic nature of the planktonic foraminifera "*Globigerinoides*", and description of the new genus Trilobatus. *PLoS ONE* **10**, e0128108 (2015).
64. Martínez-Botí, M. A. et al. Boron isotope evidence for oceanic carbon dioxide leakage during the last deglaciation. *Nature* **518**, 219–222 (2015).
65. Key, R. M. et al. A global ocean carbon climatology: results from Global Data Analysis Project (GLODAP). *Global Biogeochem. Cycles* **18**, GB4031 (2004).
66. Olsen, A. et al. GLODAPv2. 2020–the second update of GLODAPv2. *Earth Syst. Sci. Data* **12**, 3653–3678 (2020).
67. Suzuki, T. et al. *PACIFICA Data Synthesis Project* (Carbon Dioxide Information Analysis Center, 2013).
68. Schlitzer, R. Electronic atlas of WOCE hydrographic and tracer data now available. *Eos Trans.* **81**, 45 (2000).
69. Schlitzer, R. Ocean Data View. (2018). Available at: https://www.odv.awi.de.
70. Dickson, A. G., Sabine, C. L. & Christian, J. R. *Guide to Best Practices for Ocean CO_2 Measurements* (North Pacific Marine Science Organization, 2007).
71. Lewis, E. R. & Wallace, D. W. R. *Program Developed for CO_2 System Calculations* (Environmental System Science Data Infrastructure for a Virtual Ecosystem, 1998).
72. Huang, B. et al. Extended reconstructed sea surface temperature, version 5 (ERSSTv5): upgrades, validations, and intercomparisons. *J. Clim.* **30**, 8179–8205 (2017).
73. NOAA Climate Prediction Center Internet Team. Cold and Warm Episodes by Season. (2021). Available at: https://origin.cpc.ncep.noaa.gov/products/analysis_monitoring/ensostuff/ONI_v5.php. (Accessed: 22 March 2021)
74. Zeebe, R. E. & Tyrrell, T. History of carbonate ion concentration over the last 100 million years II: revised calculations and new data. *Geochim. Cosmochim. Acta* **257**, 373–392 (2019).
75. Foster, G. L. Seawater pH, pCO_2 and $[CO^{2-}_3]$ variations in the Caribbean Sea over the last 130 kyr: a boron isotope and B/Ca study of planktic foraminifera. *Earth Planet. Sci. Lett.* **271**, 254–266 (2008).
76. Kiss, E. Ion-exchange separation and spectrophotometric determination of boron in geological materials. *Anal. Chim. Acta* **211**, 243–256 (1988).
77. Okai, T., Suzuki, A., Kawahata, H., Terashima, S. & Imai, N. Preparation of a new Geological Survey of Japan geochemical reference material: Coral JCp-1. *Geostand. Newsl.* **26**, 95–99 (2002).
78. Al-Ammar, A. S., Gupta, R. K. & Barnes, R. M. Elimination of boron memory effect in inductively coupled plasma-mass spectrometry by ammonia gas injection into the spray chamber during analysis. *Spectrochim. Acta Part B At. Spectrosc.* **55**, 629–635 (2000).

79. Berner, E. K. & Berner, R. A. *Global Environment: Water, Air, and Geochemical Cycles* (Prentice-Hall, 1996).
80. Broecker, W. S. & Peng, T. S. *Tracers in the Sea* (Eldigio, 1982).
81. Fantle, M. S. & DePaolo, D. J. Sr isotopes and pore fluid chemistry in carbonate sediment of the Ontong Java Plateau: calcite recrystallization rates and evidence for a rapid rise in seawater Mg over the last 10 million years. *Geochim. Cosmochim. Acta* **70**, 3883–3904 (2006).
82. Lowenstein, T. K., Timofeeff, M. N., Brennan, S. T., Hardie, L. A. & Demicco, R. V. Oscillations in Phanerozoic seawater chemistry: evidence from fluid inclusions. *Science* **294**, 1086–1088 (2001).
83. Horita, J., Zimmermann, H. & Holland, H. D. Chemical evolution of seawater during the Phanerozoic: implications from the record of marine evaporites. *Geochim. Cosmochim. Acta* **66**, 3733–3756 (2002).
84. Chalk, T. B. et al. Causes of ice age intensification across the mid-Pleistocene transition. *Proc. Natl Acad. Sci. USA* **114**, 13114–13119 (2017).
85. Greenop, R. et al. Orbital forcing, ice volume, and CO_2 across the Oligocene-Miocene transition. *Paleoceanogr. Paleoclimatology* **34**, 316–328 (2019).
86. Sosdian, S. M., Babila, T. L., Greenop, R., Foster, G. L. & Lear, C. H. Ocean carbon storage across the middle Miocene: a new interpretation for the Monterey event. *Nat. Commun.* **11**, 134 (2020).
87. Evans, D. & Müller, W. Deep time foraminifera Mg/Ca paleothermometry: nonlinear correction for secular change in seawater Mg/Ca. *Paleoceanography* **27**, PA4205 (2012).
88. Tierney, J. E., Malevich, S. B., Gray, W., Vetter, L. & Thirumalai, K. Bayesian calibration of the Mg/Ca paleothermometer in planktic foraminifera. *Paleoceanogr. Paleoclimatology* **34**, 2005–2030 (2019).
89. Anand, P., Elderfield, H. & Conte, M. H. Calibration of Mg/Ca thermometry in planktonic foraminifera from a sediment trap time series. *Paleoceanography* **18**, 1050 (2003).
90. Gray, W. R. et al. Deglacial upwelling, productivity and CO_2 outgassing in the North Pacific Ocean. *Nat. Geosci.* **11**, 340–344 (2018).
91. Lemarchand, D., Gaillardet, J., Lewin, E. & Allegre, C. J. Boron isotope systematics in large rivers: implications for the marine boron budget and paleo-pH reconstruction over the Cenozoic. *Chem. Geol.* **190**, 123–140 (2002).
92. Simon, L., Lécuyer, C., Maréchal, C. & Coltice, N. Modelling the geochemical cycle of boron: implications for the long-term $\delta^{11}B$ evolution of seawater and oceanic crust. *Chem. Geol.* **225**, 61–76 (2006).
93. Greenop, R. et al. A record of Neogene seawater $\delta^{11}B$ reconstructed from paired $\delta^{11}B$ analyses on benthic and planktic foraminifera. *Clim. Past* **13**, 149–170 (2017).
94. Foster, G. L., Pogge von Strandmann, P. A. E. & Rae, J. W. B. Boron and magnesium isotopic composition of seawater. *Geochem. Geophys. Geosystems* **11**, Q08015 (2010).
95. Shields, C. A. et al. The low-resolution CCSM4. *J. Clim.* **25**, 3993–4014 (2012).
96. Moore, J. K., Doney, S. C. & Lindsay, K. Upper ocean ecosystem dynamics and iron cycling in a global three-dimensional model. *Global Biogeochem. Cycles* **18**, GB4028 (2004).
97. Tan, I., Storelvmo, T. & Zelinka, M. D. Observational constraints on mixed-phase clouds imply higher climate sensitivity. *Science* **352**, 224–227 (2016).
98. Erfani, E. & Burls, N. J. The strength of low-cloud feedbacks and tropical climate: a CESM sensitivity study. *J. Clim.* **32**, 2497–2516 (2019).
99. Li, R. L., Storelvmo, T., Fedorov, A. V. & Choi, Y.-S. A positive IRIS feedback: insights from climate simulations with temperature-sensitive cloud–rain conversion. *J. Clim.* **32**, 5305–5324 (2019).
100. Mauritsen, T. & Stevens, B. Missing iris effect as a possible cause of muted hydrological change and high climate sensitivity in models. *Nat. Geosci.* **8**, 346–351 (2015).
101. Williams, I. N. & Pierrehumbert, R. T. Observational evidence against strongly stabilizing tropical cloud feedbacks. *Geophys. Res. Lett.* **44**, 1503–1510 (2017).
102. Sagoo, N. & Storelvmo, T. Testing the sensitivity of past climates to the indirect effects of dust. *Geophys. Res. Lett.* **44**, 5807–5817 (2017).
103. Thomas, M. D., Fedorov, A. V., Burls, N. J. & Liu, W. Oceanic pathways of an active Pacific meridional overturning circulation (PMOC). *Geophys. Res. Lett.* **48**, e2020GL091935 (2021).
104. Blanke, B. & Raynaud, S. Kinematics of the Pacific equatorial undercurrent: an Eulerian and Lagrangian approach from GCM results. *J. Phys. Oceanogr.* **27**, 1038–1053 (1997).
105. Gent, P. R. & Mcwilliams, J. C. Isopycnal mixing in ocean circulation models. *J. Phys. Oceanogr.* **20**, 150–155 (1990).
106. Van Sebille, E. et al. Lagrangian ocean analysis: fundamentals and practices. *Ocean Model.* **121**, 49–75 (2018).
107. Arakawa, A. & Lamb, V. R. Computational design of the basic dynamical processes of the UCLA general circulation model. *Gen. Circ. Model. Atmos.* **17**, 173–265 (1977).
108. Marshall, B. J. et al. Morphometric and stable isotopic differentiation of Orbulina universa morphotypes from the Cariaco Basin, Venezuela. *Mar. Micropaleontol.* **120**, 46–64 (2015).
109. Raitzsch, M. et al. Boron isotope-based seasonal paleo-pH reconstruction for the Southeast Atlantic – a multispecies approach using habitat preference of planktonic foraminifera. *Earth Planet. Sci. Lett.* **487**, 138–150 (2018).
110. Guillermic, M. et al. Seawater pH reconstruction using boron isotopes in multiple planktonic foraminifera species with different depth habitats and their potential to constrain pH and pCO_2 gradients. *Biogeosciences* **17**, 3487–3510 (2020).
111. Bartoli, G., Hönisch, B. & Zeebe, R. E. Atmospheric CO_2 decline during the Pliocene intensification of Northern Hemisphere glaciations. *Paleoceanography* **26**, PA4213 (2011).
112. Hönisch, B., Hemming, N. G., Archer, D., Siddall, M. & McManus, J. F. Atmospheric carbon dioxide concentration across the mid-Pleistocene transition. *Science* **324**, 1551–1554 (2009).
113. Seki, O. et al. Alkenone and boron-based Pliocene pCO_2 records. *Earth Planet. Sci. Lett.* **292**, 201–211 (2010).
114. Sosdian, S. M. et al. Constraining the evolution of Neogene ocean carbonate chemistry using the boron isotope pH proxy. *Earth Planet. Sci. Lett.* **498**, 362–376 (2018).
115. de la Vega, E., Chalk, T. B., Wilson, P. A., Bysani, R. P. & Foster, G. L. Atmospheric CO_2 during the mid-Piacenzian warm period and the M2 glaciation. *Sci. Rep.* **10**, 11002 (2020).
116. Medina-Elizalde, M. & Lea, D. W. The mid-Pleistocene transition in the tropical Pacific. *Science* **310**, 1009–1012 (2005).
117. Liu, Z. & Herbert, T. D. High-latitude influence on the eastern equatorial Pacific climate in the early Pleistocene epoch. *Nature* **427**, 720–723 (2004).
118. Regenberg, M. et al. Global dissolution effects on planktonic foraminiferal Mg/Ca ratios controlled by the calcite-saturation state of bottom waters. *Paleoceanography* **29**, 127–142 (2014).
119. Pagani, M., Liu, Z., LaRiviere, J. & Ravelo, A. C. High Earth-system climate sensitivity determined from Pliocene carbon dioxide concentrations. *Nat. Geosci.* **3**, 27–30 (2010).
120. Conte, M. H. et al. Global temperature calibration of the alkenone unsaturation index (UK′ 37) in surface waters and comparison with surface sediments. *Geochem. Geophys. Geosystems* **7**, Q02005 (2006).
121. Kim, J.-H. et al. New indices and calibrations derived from the distribution of crenarchaeal isoprenoid tetraether lipids: implications for past sea surface temperature reconstructions. *Geochim. Cosmochim. Acta* **74**, 4639–4654 (2010).
122. Evans, D., Brierley, C., Raymo, M. E., Erez, J. & Müller, W. Planktic foraminifera shell chemistry response to seawater chemistry: Pliocene–Pleistocene seawater Mg/Ca, temperature and sea level change. *Earth Planet. Sci. Lett.* **438**, 139–148 (2016).
123. Coggon, R. M., Teagle, D. A. H., Smith-Duque, C. E., Alt, J. C. & Cooper, M. J. Reconstructing past seawater Mg/Ca and Sr/Ca from mid-ocean ridge flank calcium carbonate veins. *Science* **327**, 1114–1117 (2010).
124. Rausch, S., Böhm, F., Bach, W., Klügel, A. & Eisenhauer, A. Calcium carbonate veins in ocean crust record a threefold increase of seawater Mg/Ca in the past 30 million years. *Earth Planet. Sci. Lett.* **362**, 215–224 (2013).
125. Dekens, P. S., Lea, D. W., Pak, D. K. & Spero, H. J. Core top calibration of Mg/Ca in tropical foraminifera: refining paleotemperature estimation. *Geochemistry, Geophys. Geosystems* **3**, 1–29 (2002).
126. Müller, P. J., Kirst, G., Ruhland, G., Von Storch, I. & Rosell-Melé, A. Calibration of the alkenone paleotemperature index U37K′ based on core-tops from the eastern South Atlantic and the global ocean (60° N-60° S). *Geochim. Cosmochim. Acta* **62**, 1757–1772 (1998).

Acknowledgements The authors acknowledge and appreciate the aid of J. Robbins, W. Strojie, D. Asael and S. Zhang in supervising clean lab chemistry, boron and trace element analysis, and data processing. The authors also appreciate discussion with J. Rae. This work was supported by NSF Award 1602557 and 170251 to P.M.H., NSF Award 1844380 and 2002448 to N.J.B. and Sloan Ocean Fellowships to P.M.H. and N.J.B. Additional funding to A.V.F. was provided by the Guggenheim Fellowship and the ARCHANGE project (ANR-18-MPGA-0001, France). We acknowledge high-performance computing support from Cheyenne (https://doi.org/10.5065/D6RX99HX) provided by NCAR's Computational and Information Systems Laboratory, sponsored by the NSF.

Author contributions M.S. contributed: study design, boron and trace element data collection, data analysis, writing, editing. N.B. contributed: study design, model simulations, writing, editing. A.F. contributed: supervision, writing, editing. M.T. contributed: model simulations, Lagrangian analysis, editing. W.L. contributed: Lagrangian analysis. D.P. contributed: data analysis, supervision, editing. HF contributed: BAYMAG SST data processing, editing. P.J. contributed: model simulations. N.P. contributed: study design, supervision, writing, editing. P.H. contributed: study design, supervision, writing, editing.

Competing interests The authors declare no competing interests.

Additional information

Supplementary information The online version contains supplementary material available at https://doi.org/10.1038/s41586-021-03884-7.

Correspondence and requests for materials should be addressed to Madison G. Shankle or Pincelli M. Hull.

Peer review information *Nature* thanks Kelsey Dyez, Julia Tindall and the other, anonymous, reviewer(s) for their contribution to the peer review of this work. Peer reviewer reports are available.

Reprints and permissions information is available at http://www.nature.com/reprints.

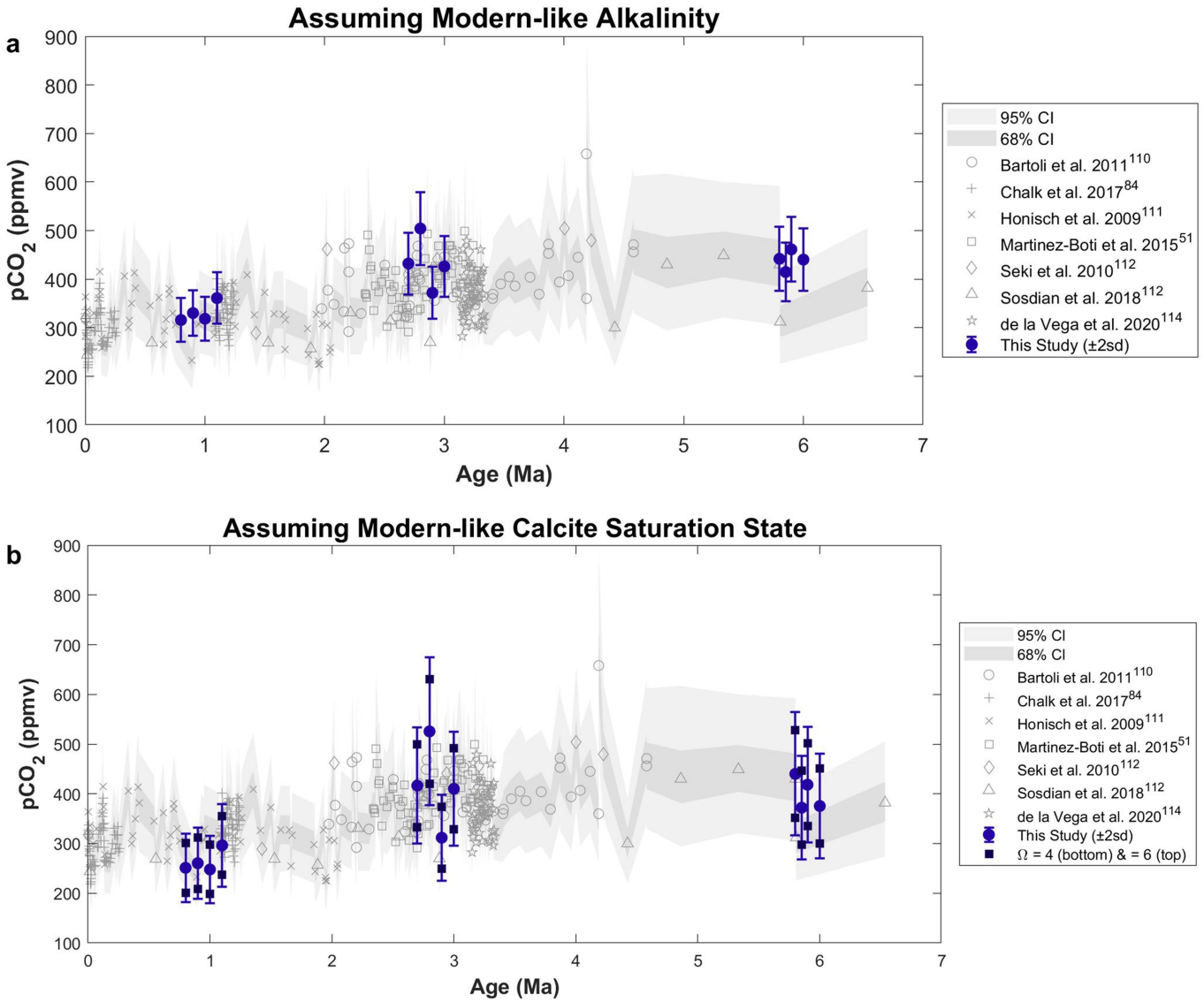

Extended Data Fig. 1 | pCO_2 from this study's western equatorial Pacific (WEP) pH values match previous $\delta^{11}B$-derived studies. a, **b**, pCO_2 estimates (blue markers and shaded areas showing 68% and 95% confidence intervals) from this study's pH data from the WEP, a region in equilibrium with the atmosphere[37], assuming a modern-like alkalinity of 2,275 ± 200 µmol kg^{-1} (**a**) versus a modern-like calcite saturation state ($\Omega = 5 \pm 2$ (error bars), $\Omega = 4$ (lower black squares) and $\Omega = 6$ (upper black squares); **b**). Grey data points show $\delta^{11}B$-deried estimates of pCO_2 from previously published studies, with shading showing reported confidence intervals[51,84,111–115].

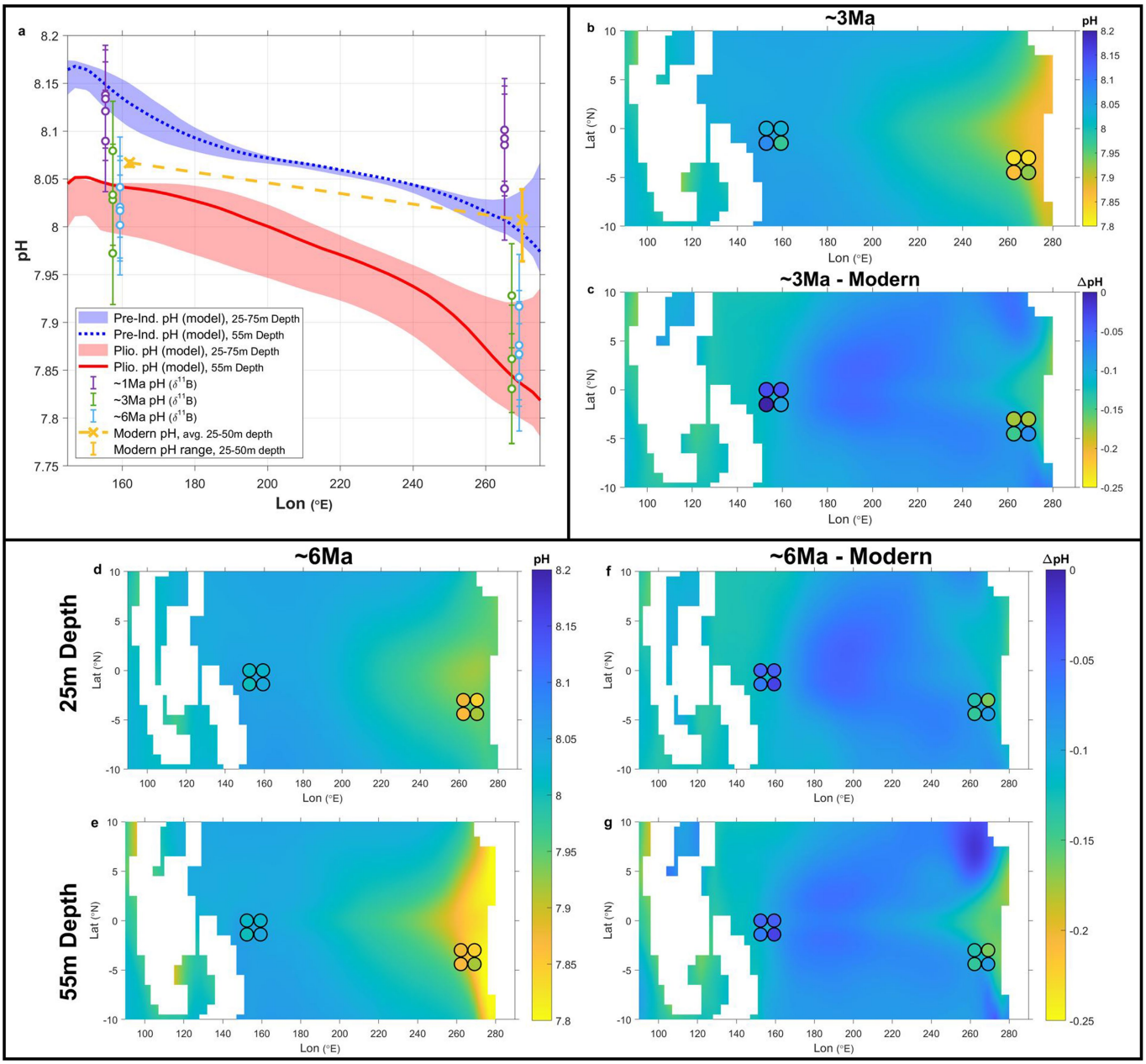

Extended Data Fig. 2 | δ^{11}B-reconstructed pH matches model output over 25–75 m depth (top left, bottom); reconstructed pH data from ~3 Ma compared to model output also provided for reference (top right). **a**, Modelled pH along the equator (at 55 m depth (red solid and blue dashed lines) and across the 25–75 m depth range (shaded areas)) and δ^{11}B-derived pH (circles with 2σ uncertainty from a Monte Carlo simulation, as in Fig. 2b). Markers placed at their approximate longitudes (159.362°E for western ODP Site 806 and 269.182°E for eastern ODP Site 846). The observed (see Methods) modern gradient in surface pH averaged across the 25–50 m depth range is included for reference (yellow crosses), as well as the range of pH from available modern observations (vertical yellow bars on crosses). **b**–**g**, Climatological model output of pH and d^{11}B-reconstructed pH with proxy data (circles) from ~3 Ma instead of ~6 Ma (**b**, **c**) and model output (contours) at distinct depths of 25 m ad 55 m (bracketing *O. universa*'s depth habitat) instead of averaged over the 25–55 m range (**d**–**g**). In all panels, more acidic waters (or more acidic waters in the past) are shown in yellow-green colours.

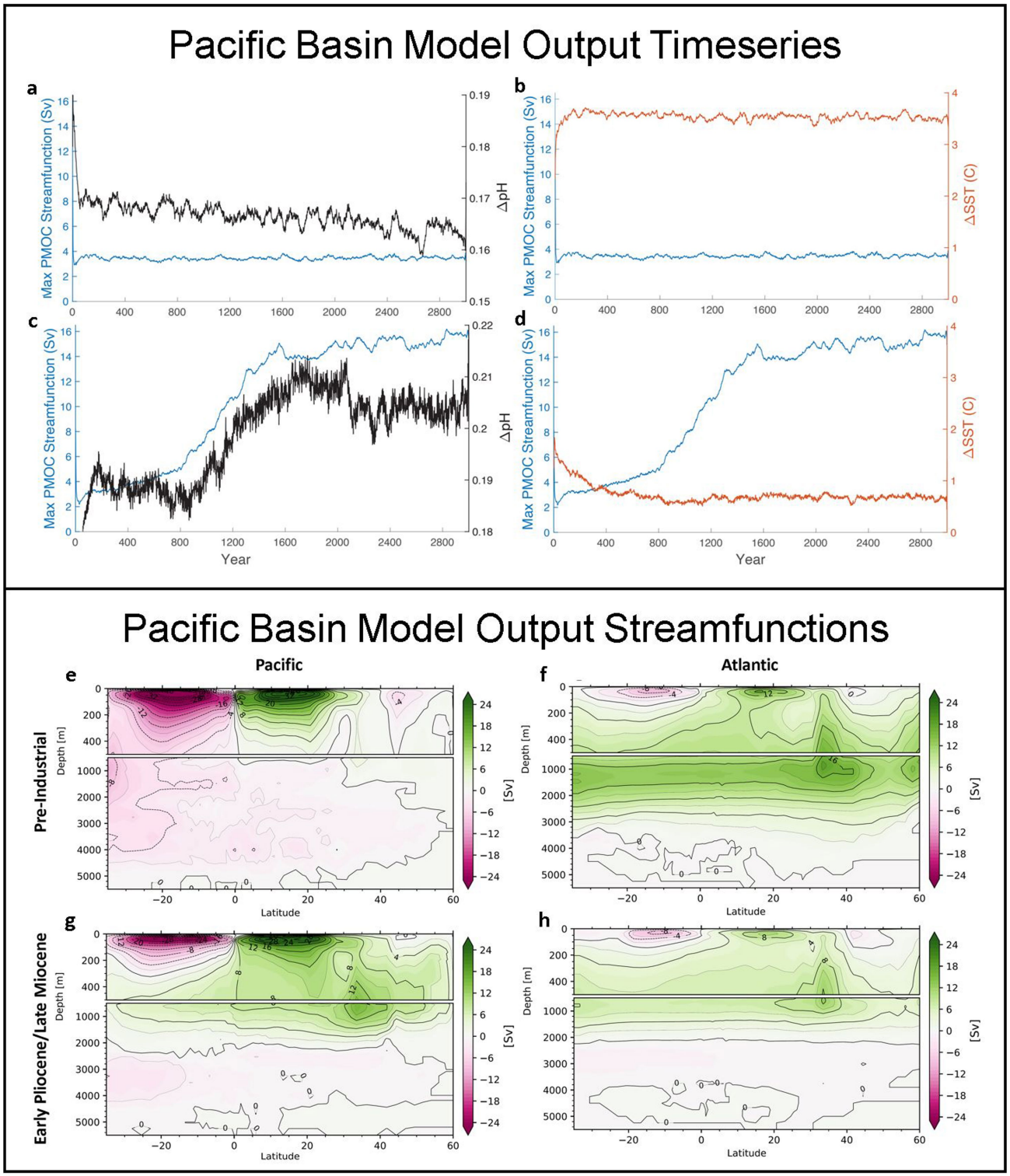

Extended Data Fig. 3 | Extended physical oceanographic model output links pH changes to a Pacific meridional overturning circulation. **a**–**d**, Timeseries of PMOC strength (blue lines), zonal Pacific pH gradient (ΔpH, black lines), and zonal Pacific SST gradient (ΔSST, red lines) for the model control run (**a**, **b**) and early Pliocene/late Miocene run (**c**, **d**). PMOC strength (Max PMOC Streamfunction) is defined as the maximum streamfunction north of 25°N and below 500 m depth in sverdrups (1 Sv = 10^6 m^3 s^{-1}). The pH gradient is defined as the pH difference between a western (5°S–5°N, 150–170°E) and eastern Pacific box (5°S–5°N, 260–280°E), taken at 55 m depth. The SST gradient is defined as the SST difference between the same boxes taken at the surface. Note that while the zonal SST gradient equilibrates within ~500 years in the early Pliocene/late Miocene experiment (**d**) and is hardly influenced by the appearance of the PMOC between ~800–1,600 years, the zonal pH gradient increases in phase with the PMOC (**c**). **e**–**h**, Zonally averaged streamfunction over the Pacific (**e**, **g**) and Atlantic (**f**, **h**) basins for the control run (**e**, **f**) and early Pliocene/late Miocene (**g**, **h**) runs of the model Positive (green values) denote clockwise circulation, and negative (pink) values denote counterclockwise rotation. Panel **g** is the same as Fig. 4b in the main text.

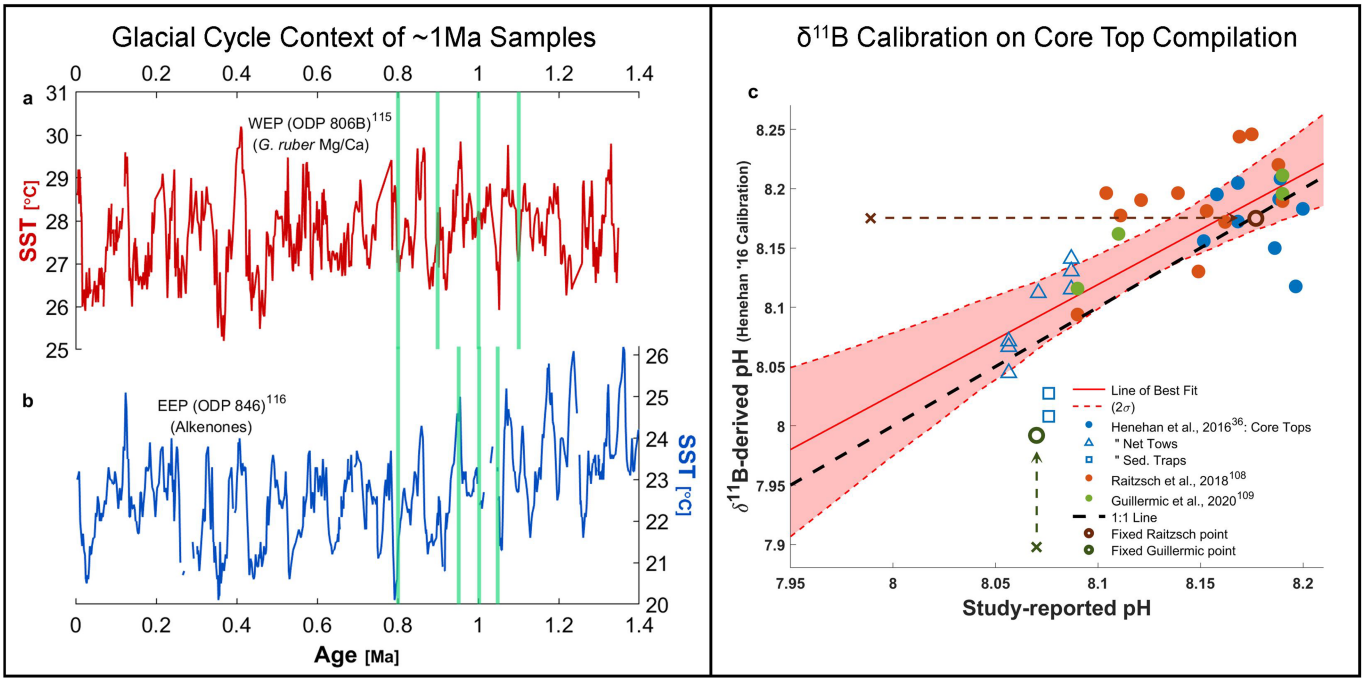

Extended Data Fig. 4 | This study's ~1 Ma samples fall in different stages of the glacial–interglacial cycles, and δ^{11}B-pH core top calibration used in this study recreates observed ambient pH. a, **b**, High-resolution sea surface temperature records from western equatorial Pacific site ODP 806 *G. ruber*-derived Mg/Ca data[116] (**a**) and eastern equatorial Pacific ODP Site 846 alkenone ($U^{K'}_{37}$) data[117] (**b**). In both panels the ages of the ~1 Ma samples in this study are overlain as green lines, falling at different points in the glacial–interglacial cycles. **c**, Core top, net tow, and sediment trap $d^{11}B$ data[36,109,110] converted to pH using the calibration of Henehan et al.[36] shows good agreement with reported in situ pH. For the odd point to the far right (dark orange, *x*), Raitzsch et al[109]. calculated in situ pH using an anomalous low value of alkalinity (~200 µmol kg^{-1} lower than alkalinity for the location reported in datasets such as GLODAPv2[66]. Recalculating pH using the same in situ temperature and salinity as Raitzsch et al. but an alkalinity value derived from GLODAPv2 (2,325 µmol kg^{-1}) brings the point in agreement with the other data (empty dark orange circle). For the odd point in the lower part of the figure (dark green, *x*), Guillermic and colleagues[110]. report an unrealistic value for temperature at this site: ~18 °C whereas the same site (in the central Indian Ocean) appears to be closer to ~26 °C on average according to GLODAPv2. When we re-calculate δ^{11}B-pH derived pH using GLODAPv2's 26 °C, this brings the point into better agreement with the other data (empty dark green circle). The line of best fit and 2σ shading was calculated with the original odd data points, however, and note that the core top data is still in good agreement with reported in situ pH following this calibration.

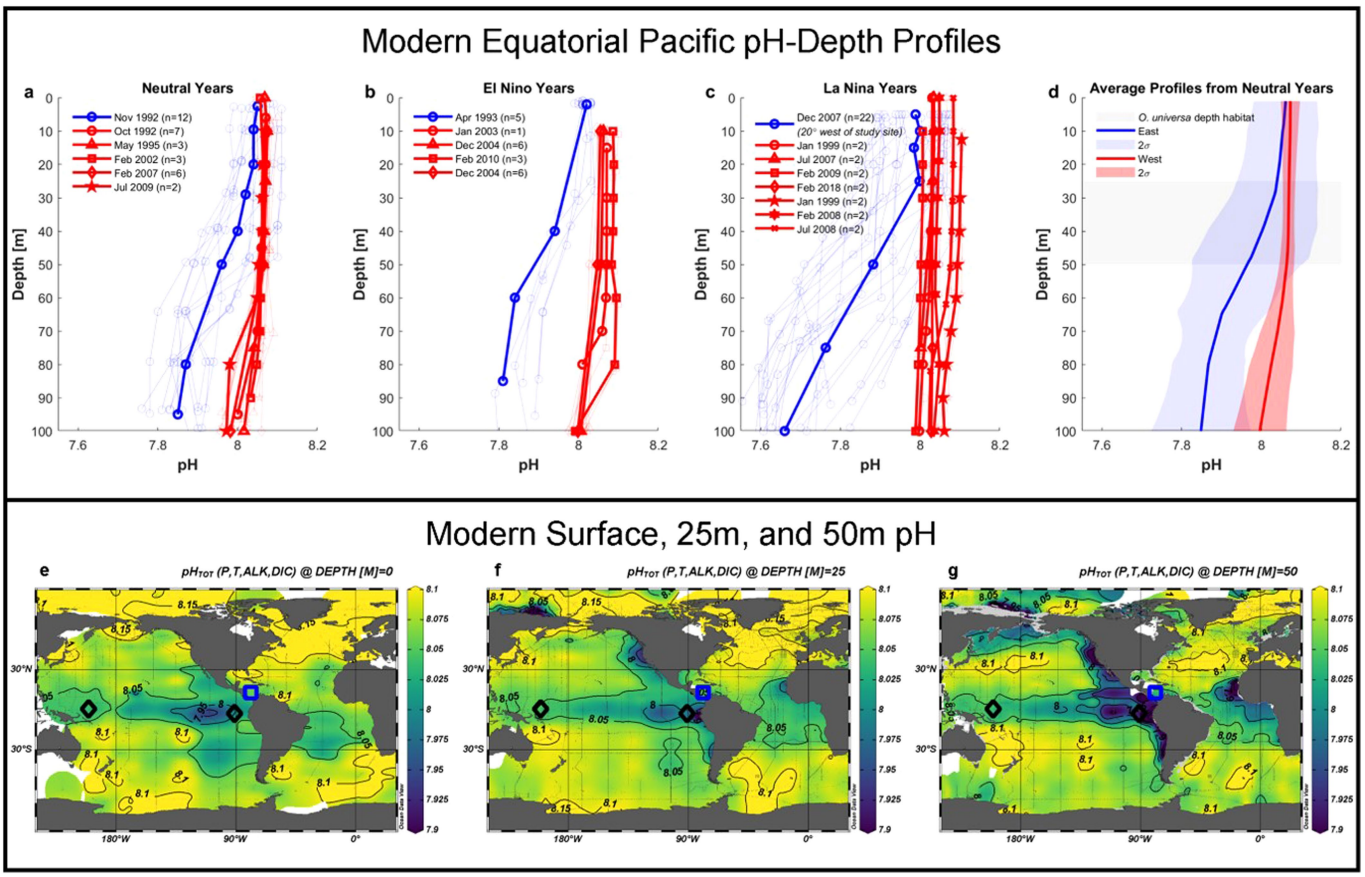

Extended Data Fig. 5 | Modern observational pH shows modest zonal pH gradients. a–**d**, Observed pH (or pH calculated from alkalinity and total dissolved inorganic carbon (DIC)) from all cruises within 5° latitude and longitude of our study sites (pale profiles) during neutral-ENSO (**a**), El Niño (**b**) and La Niña conditions (**c**). Thick lines in panels **a**–**c** show average profiles from all stations on a given cruise. **d**, Average pH-depth profiles from all neutral-ENSO observations. Modern reference values of pH (that is, diamonds on the *y* axis in Fig. 2) were derived from averaging panel **d**'s profiles over 25–50 m depth (approximate depth habitat of *O. universa*). **e**–**g**, Modern pH derived from cruise-based observations of alkalinity and total DIC. Data compiled from the GLODAPv2 dataset[66] and plotted using the Ocean Data View software (R. Schlitzer, Ocean Data View, https://www.osv.awi.de, 2018). Overlain are this study's sites (black diamonds) as well as the site of the additional 3 Ma pH values[51] included in Fig. 2 (blue square).

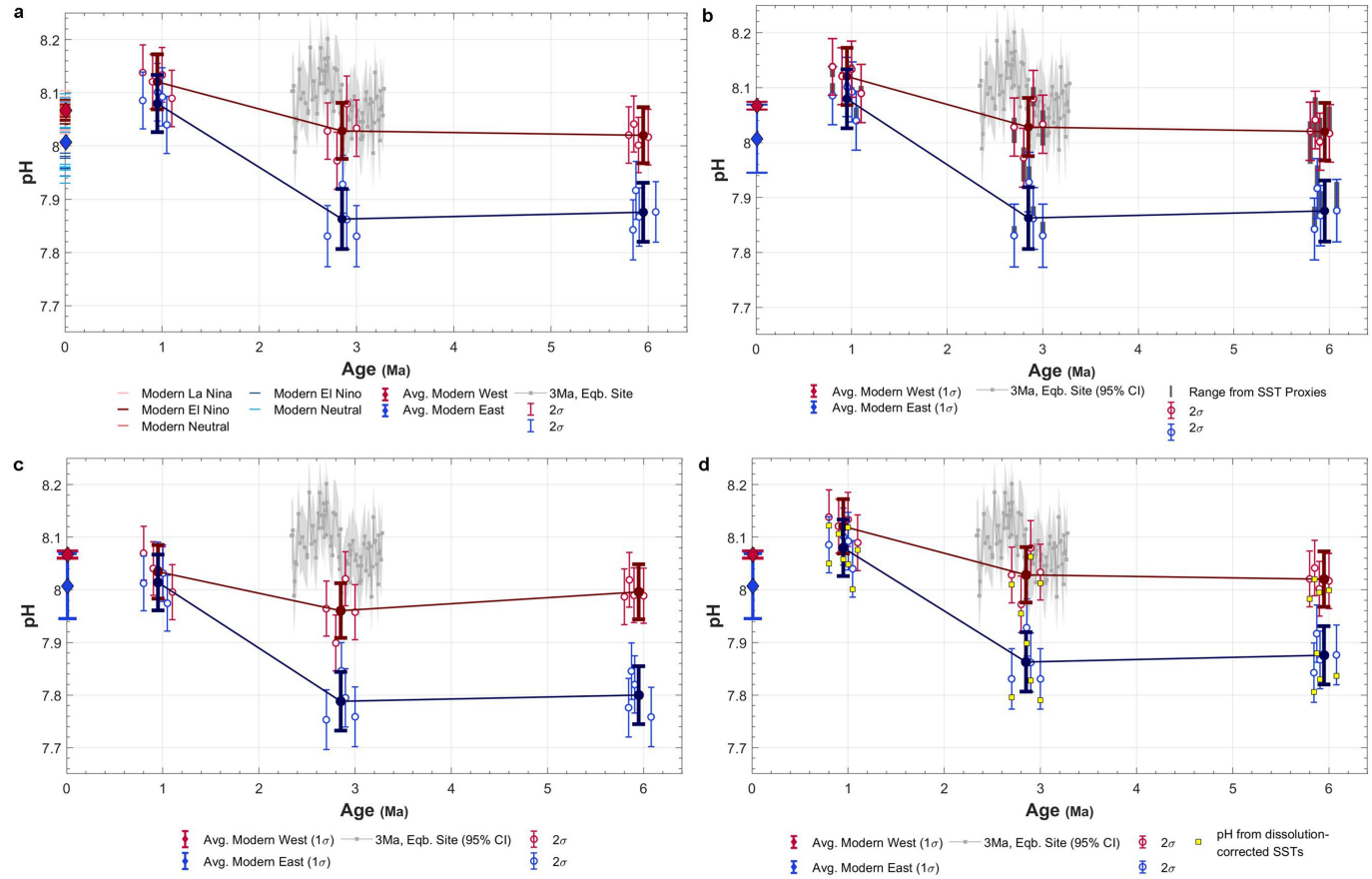

Extended Data Fig. 6 | An enhanced early Pliocene/late Miocene zonal pH gradient is observed under different treatments of the data. δ^{11}B-derived pH from *O. universa* from the east (blue) and west (red) with 2σ uncertainty from a Monte Carlo simulation (empty circles; averages at ~1 Ma, ~3 Ma and ~6 Ma in filled circles) showing: all observations of modern pH used in producing average modern pH reference values (diamonds) given as individual dashes (**a**), the range of pH from using varied SST records in the pH calculation (grey bars) (**b**), pH as calculated using the SST record derived from calibrating this study's Mg/Ca data with the BAYMAG calibration[88] (**c**), and pH as calculated using dissolution-corrected[118] Mg/Ca SSTs from this study (yellow squares) (**d**). In panel **b**, pH ranges cover pH calculated using: TEX86-derived[3] SSTs, Mg/Ca-derived SSTs (this study) using a linear correction for Mg/Ca_{sw}, and Mg/Ca-derived SSTs (this study) using a power-law correction[87] for Mg/Ca_{sw}. Both Mg/Ca-SST calibrations were done using the Mg/Ca_{sw} record of Fantle and DePaolo[81].

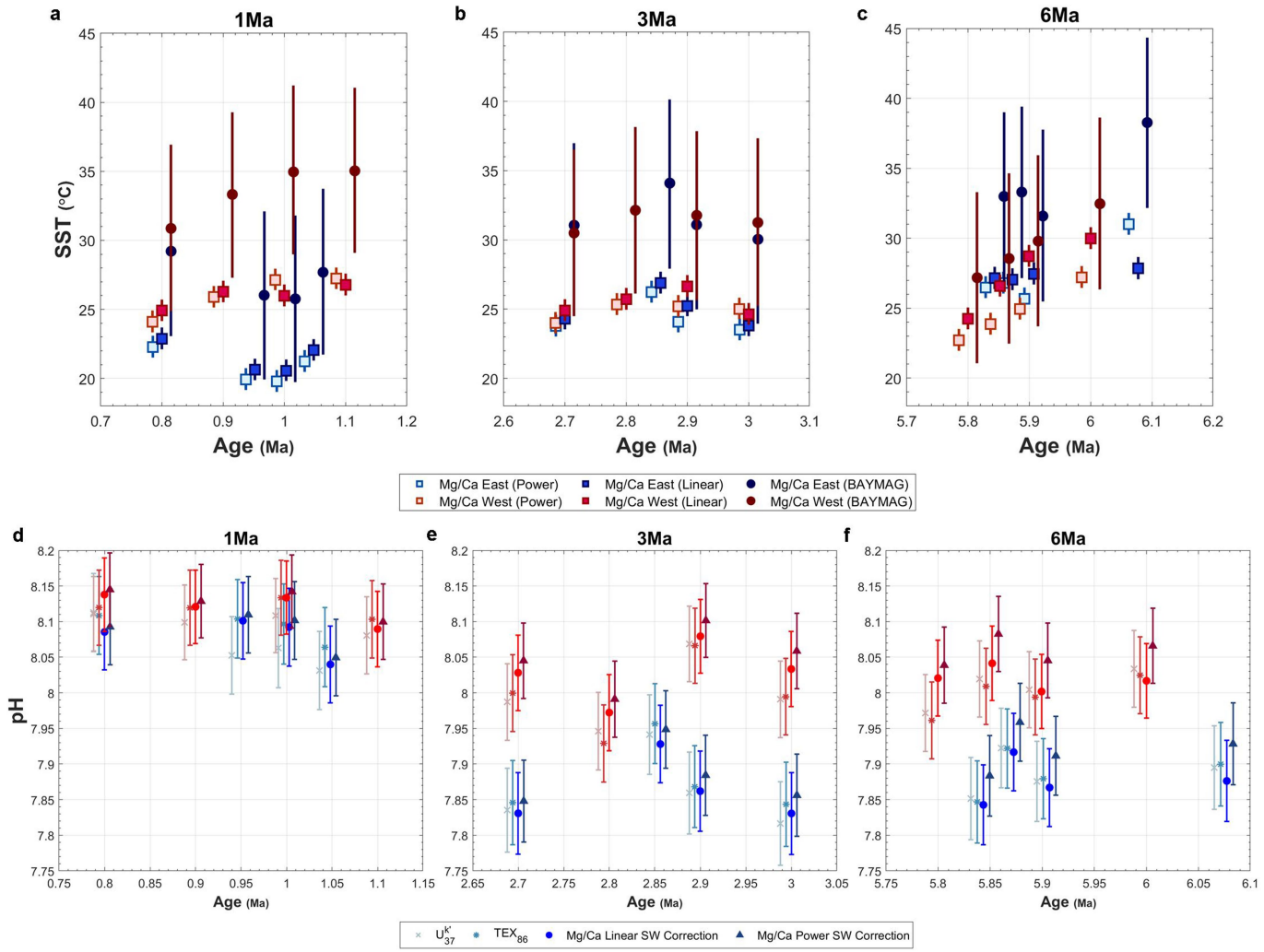

Extended Data Fig. 7 | Choice of Mg/Ca calibration or even SST proxy has little effect on pH. a–**c**, Mg/Ca-derived SSTs for eastern (blue) and western (red) equatorial Pacific at ~1 Ma, ~3 Ma and ~6 Ma calculated using the *O. universa* calibration of Anand et al.[89], using a linear (dark squares) and power-law (light squares) relationship between Mg/Ca_{SW} and Mg/Ca_{test}, and using the Bayesian calibration BAYMAG[88], also corrected for Mg/Ca_{SW}. Error bars denote calibration errors on *O. universa* calibration (squares) and 95% confidence intervals on the BAYMAG-calibrated data (circles). Dark squares are plotted at corrects ages; other markers are offset for ease of viewing. **d**–**f**, $\delta^{11}B$-derived pH at the time points calculated using SST records from $U^{K'}_{37}$[7,119] (crosses, using the SST calibration of Conte et al.[120]), TEX_{86}[3] (asterisks, using the SST calibration of Kim et al.[120]), and Mg/Ca data (this study, using the *O. universa* SST calibration of Anand et al.[89]) (assuming a linear (circles) and power-law[87] (triangles) relationship between Mg/Ca_{SW} and Mg/Ca_{test}). Note that because the western-site $U^{K'}_{37}$ record[119] (red crosses, bottom panels) only extends back to ~5.3 Ma, we assume the maximum temperature calculable by this calibration (~28.5 °C[121]) for our western points at ~6 Ma (red crosses, panel **f**), towards which the record of Pagani et al.[119] was trending and had nearly approached even by ~5.3 Ma (~28.3–28.4 °C)). All error bars on pH depict uncertainty (2σ) returned from a Monte Carlo simulation.

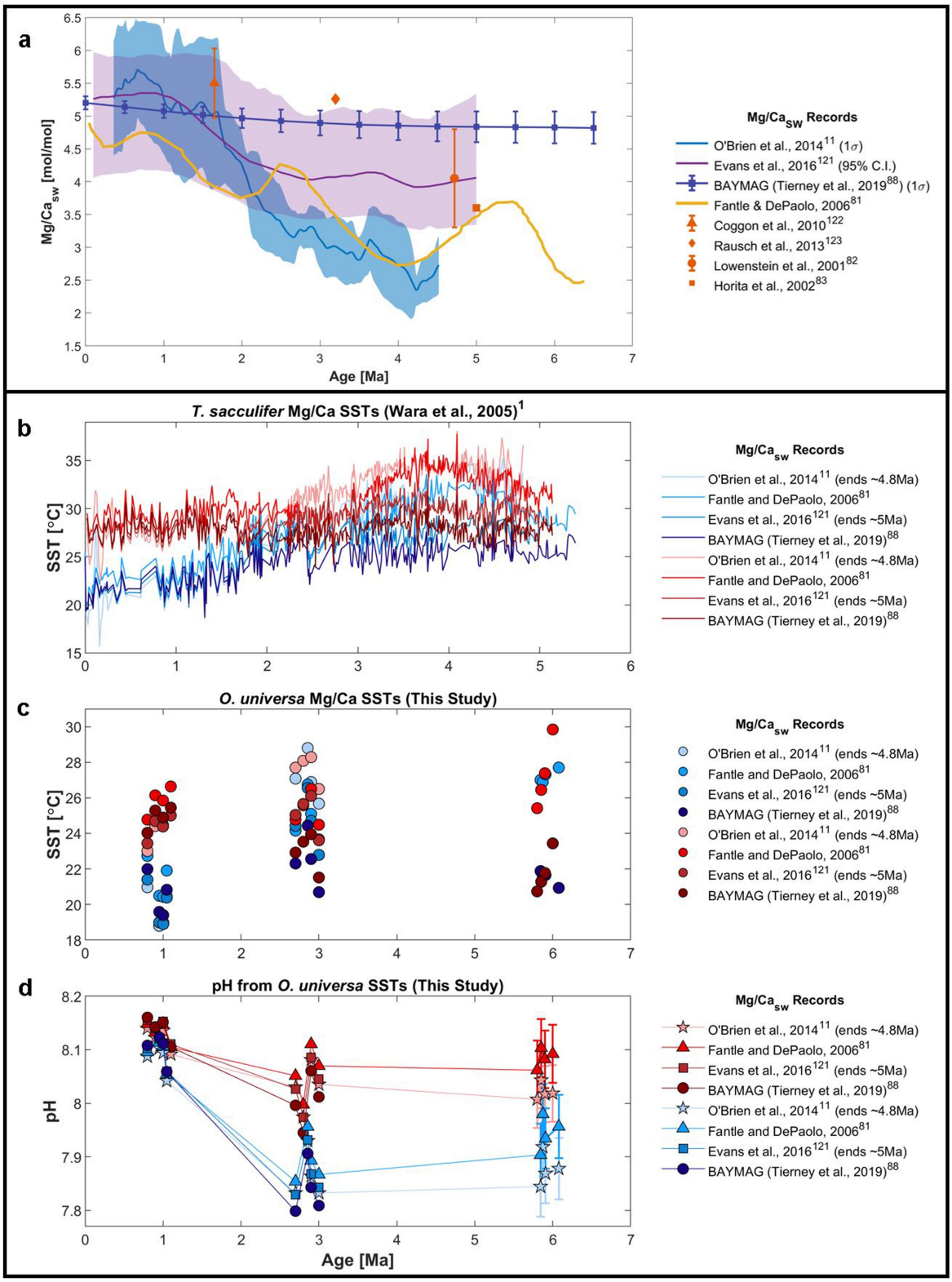

Extended Data Fig. 8 | Different $Mg/Ca_{seawater}$ records influence sea surface temperatures but have only a modest impact on pH. a, Various published Mg/Ca_{SW} reconstructions[11,81,88,122] (lines) plotted alongside proxy-based estimates (orange points) from carbonate veins[123,124] (orange triangle and diamond) and fluid inclusions[82,83] (orange circle and square) with error reported in those studies (where there are error bars). **b**–**d**, Using different Mg/Ca_{SW} records only slightly affect SSTs and even less so pH results. **b**, SSTs calculated from *T. sacculifer* Mg/Ca data[1] using the species-specific calibration of Dekens et al.[125] and various Mg/Ca_{SW} reconstructions[11,81,88,122]. **c**, SSTs calculated from *O. universa* Mg/Ca data (this study) using the species-specific calibration of Anand et al.[89] a and various Mg/Ca_{SW} reconstructions[11,81,88,122]. **d**, $\delta^{11}B$-derived pH (this study) using the various SST reconstructions in panel **c**. Note that the Mg/Ca_{SW} records of O'Brien et al.[11] and Evans et al.[122] (blue and purple lines in panel **a**) do note extend back far enough to apply to the ~6 Ma data, ending at ~4.8 Ma and ~5 Ma, respectively.

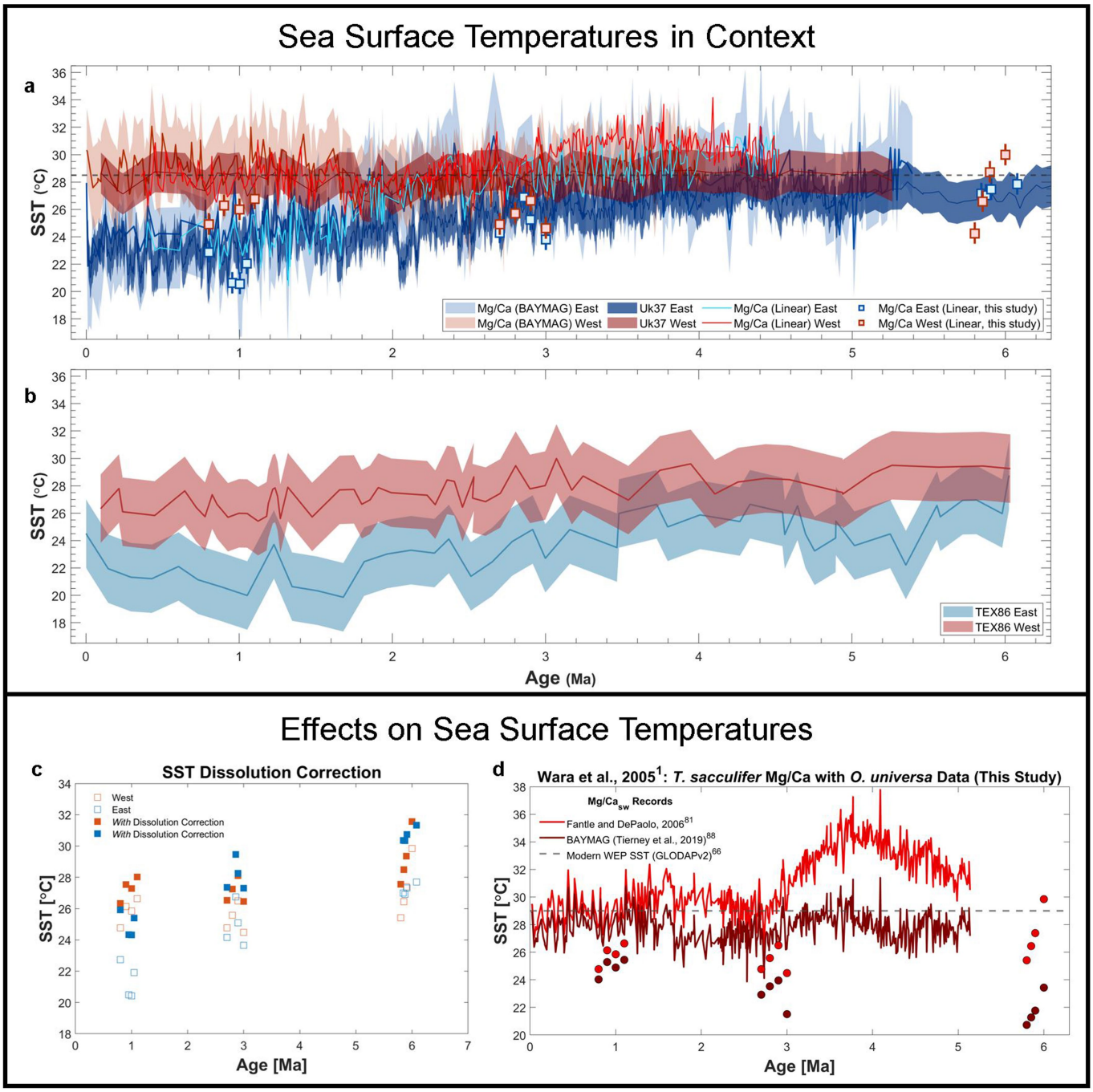

Extended Data Fig. 9 | Different sea surface temperature proxies record varying reductions in the zonal sea surface temperature gradient, and a dissolution correction and different Mg/Ca_{sw} record is applied to this study's data. a, **b**, SST records from the eastern (blue) and western (red) equatorial Pacific. **a**, SST records which evince a collapse of the modern zonal SST gradient include: *T. sacculifer* Mg/Ca data[1] calibrated and corrected for Mg/Ca_{sw} with the Bayesian BAYMAG calibration[88] with 95% confidence intervals (pale blue and red bands); $U^{K'}_{37}$ data[7,119] using a global ocean annual-mean calibration[126] with its associated 1 s.e. (±1.1 °C) (dark blue and red bands, dashed line shows upper saturation limit of the proxy); *T. sacculifer* Mg/Ca data[1] using a species-specific calibration[125] and corrected for Mg/Ca_{sw} by O'Brien et al.[11] (bright blue and red lines, no uncertainty reported); and *O. universa* Mg/Ca data (this study) using a species-specific calibration[89] and the Mg/Ca_{sw} record of Fantle and DePaolo[81], assuming a linear relationship between Mg/Ca_{sw} and Mg/Ca_{test} (square markers with calibration error in error bars). Note that the three Mg/Ca records in this panel all use different Mg/Ca_{sw} records[11,81,88]. As the goal of this figure is to depict the range of temperature (and temperature gradient) reconstructions from the literature, we have not standardized them all to the same Mg/Ca_{sw} record. **b**, SST records which evince the modern zonal SST gradient being roughly maintained back into the early Pliocene/late Miocene, derived from TEX_{86} data[3] using the calibration of Kim et al.[121], with its associated calibration error (±2.5 °C) (blue and red bands). **c**, SSTs calculated from *O. universa* Mg/Ca data in this study both with (solid squares) and without (empty squares) applying the dissolution correction of Regenberg and colleagues[118]. **d**, Western equatorial Pacific (WEP) SSTs according to *T. sacculifer* Mg/Ca data[1] (lines) versus *O. universa* (this study, points). Depending on choice of Mg/Ca_{sw} record (light versus darker colours), even *T. sacculifer* may record cooler-than-modern temperatures in the WEP. Average annual modern WEP SST (from GLODAPv2[66]) given in the dashed line.

Extended Data Table 1 | Past literature categorizes *O. universa* as a mixed layer-dwelling species

Reference	Reported Depth Habitat
Anand et al. (2003)[89]	~50-100m
Henehan et al. (2016)[36]	Mixed layer, but can be found deeper (near thermocline, 100+ m)
Marshall et al. (2015)[107]	~25-50m
Rebotim et al. (2017)[43]	~75m
Raitzsch et al. (2018)[108]	~0-50m
Guillermic et al. (2020)[109]	Mixed layer

O. universa is a mixed layer-dwelling species[36,43,89,108–110].